

AN ABSTRACT OF THE DISSERTATION OF

Joseph H. Haxel for the degree of Doctor of Philosophy in Geology presented on November 20, 2013.

Title: Submarine Earthquakes, Volcanic Eruptions and Ambient Noise in the Northeast Pacific

Abstract approved:

Andrew J. Meigs

Robert P. Dziak

Passive hydrophone technologies and a variety of acoustic methods are applied in the deep-ocean and shallow water coastal environments of the northeast Pacific. A catalog derived from U.S. Navy regional hydrophone array recordings of acoustic *T*-phases from seafloor earthquakes is examined, describing space/time patterns through empirical orthogonal function analysis of seismicity occurring along the spreading ridges and transform fault boundaries of the Juan de Fuca plate system from 1991-2002. A small, local array of ocean bottom hydrophones (OBH) deployed in 2006 at Axial Seamount on the Juan de Fuca ridge provides an acoustic record of building microseismicity preceding the most recent magmatic dike intrusion event in April 2011. Lastly, a year of acoustic recordings (2010-2011) from a seafloor hydrophone moored in the energetic, shallow coastal environment off the central coast of Oregon result in the first long-term, low frequency (10-840 Hz) ambient noise level measurements and baseline sound budget for the inner continental shelf waters of the northeast Pacific. The successful combination of passive acoustic techniques used in

these studies displays a few of the advantages afforded by the efficient underwater transmission of acoustic energy in the marine environment.

©Copyright by Joseph H. Haxel
November 20, 2013
All Rights Reserved

Submarine Earthquakes, Volcanic Eruptions and Ambient Noise in the Northeast
Pacific

by
Joseph H. Haxel

A DISSERTATION

submitted to

Oregon State University

in partial fulfillment of
the requirements for the
degree of

Doctor of Philosophy

Presented November 20, 2013
Commencement June 2014

Doctor of Philosophy dissertation of Joseph H. Haxel presented on November 20, 2013.

APPROVED:

Co-Major Professor, representing Geology

Co-Major Professor, representing Geology

Dean of the College of Earth Ocean and Atmospheric Sciences

Dean of the Graduate School

I understand that my dissertation will become part of the permanent collection of Oregon State University libraries. My signature below authorizes release of my dissertation to any reader upon request.

Joseph H. Haxel, Author

ACKNOWLEDGEMENTS

I would like to express my sincere gratitude for the opportunity to pursue this research and graduate degree afforded me by my research advisor Dr. Robert “Bob” Dziak. I have learned a lot from Bob and greatly appreciate his mentorship, enthusiasm for science and discovery, and ability to see the “big picture” and what we can learn about the earth through all of the details. I also thank Dr. Haru Matsumoto for invaluable technical discussions and instrument support, Matt Fowler for logistical assistance, T-K “Andy” Lau for help with programming and data analysis, and Dr. Andrew Meigs for his academic support.

I thank my parents Del and Mary Lou Haxel for their encouragement and unwavering support, especially my mother who’s words “Your PhD is for you” and “Education is never a waste of time” helped to inspire and motivate me through this endeavor. I thank my children Henry and Agnes for helping to keep my perspective on the most important things, inspiring me to complete this degree and become better at using every second of the day. Most importantly, I thank my wife and best friend Jes for her patience and encouragement. I am deeply grateful for the love, support and companionship she continues to share with me every day.

CONTRIBUTION OF AUTHORS

Dr. Robert P. Dziak was involved in the analysis and writing of each manuscript of this dissertation. Dr. William W. Chadwick and Dr. Scott L. Nooner were involved in the analysis and writing of Chapter 3. T-K Lau assisted in programming and analysis for Chapter 3. Dr. Haru Matsumoto was involved in the analysis and writing of Chapter 4 of this manuscript.

TABLE OF CONTENTS

	<u>Page</u>
1 INTRODUCTION	1
1.1 REFERENCES.....	3
2 MID-OCEAN RIDGE AND TRANSFORM EARTHQUAKE VARIABILITY IN THE NORTHEAST PACIFIC.....	5
2.1 ABSTRACT.....	6
2.2 INTRODUCTION	7
2.3 DATA.....	8
2.4 BASIC EARTHQUAKE PATTERNS	10
2.4.1 <i>Ridges versus transform earthquakes</i>	10
2.4.2 <i>Time dependent regional earthquake rate changes</i>	12
2.5 EMPIRICAL ORTHOGONAL FUNCTION (EOF) ANALYSIS	13
2.5.1 <i>Eigenfunction methods</i>	13
2.5.2 <i>Regional EOF earthquake patterns</i>	17
2.5.3 <i>Segment scale EOF earthquake patterns</i>	17
2.6 DISCUSSION	21
2.7 CONCLUSIONS.....	22
2.8 REFERENCES.....	37
3 SEISMIC CYCLES, SEAFLOOR DEFORMATION AND VOLCANIC ERUPTIONS AT AXIAL SEAMOUNT, JUAN DE FUCA RIDGE	40
3.1 ABSTRACT.....	41
3.2 INTRODUCTION	41
3.3 BACKGROUND	42

TABLE OF CONTENTS (Continued)

	<u>Page</u>
3.4 METHODS	44
3.4.1 <i>Instrumentation and data</i>	44
3.4.2 <i>Hypocentral estimates</i>	45
3.5 RESULTS AND DISCUSSION	46
3.5.1 <i>Seismic cycles</i>	46
3.5.2 <i>Microearthquake locations</i>	47
3.5.3 <i>Microearthquakes and seafloor deformation</i>	48
3.6 SUMMARY	49
3.7 REFERENCES.....	56
4 OBSERVATIONS OF SHALLOW WATER MARINE AMBIENT SOUND: THE LOW FREQUENCY UNDERWATER SOUNDSCAPE OF THE CENTRAL OREGON COAST	58
4.1 ABSTRACT.....	59
4.2 INTRODUCTION	59
4.3 BACKGROUND	61
4.4 DATA AND INSTRUMENTATION.....	62
4.5 SOUND SOURCES.....	65
4.5.1 <i>Breaking surf</i>	65
4.5.2 <i>Flow noise</i>	67
4.5.3 <i>Wind</i>	68
4.5.4 <i>Rainfall</i>	69
4.5.5 <i>Biological sounds</i>	70
4.5.6 <i>Ship noise</i>	71

TABLE OF CONTENTS (Continued)

	<u>Page</u>
4.5.7 <i>Comparison of sound sources</i>	73
4.6 AMBIENT NOISE ANALYSIS	74
4.6.1 <i>Spectral averages</i>	74
4.6.2 <i>Total sound pressure levels</i>	77
4.7 DISCUSSION	78
4.8 CONCLUSIONS	79
4.9 REFERENCES	94
5 SUMMARY	98
BIBLIOGRAPHY	102

LIST OF FIGURES

<u>Figure</u>	<u>Page</u>
2.1 A decade of <i>T</i> -phase derived epicenters from the SOSUS hydroacoustic catalog spanning the period from September 1991 - January 2002	24
2.2 A map of the time averaged mean value of earthquakes per month in each spatially binned (10°x10°) area from the SOSUS earthquake catalog (1991-2002)	25
2.3 A map of skewness from the distribution of monthly earthquake counts within each grid cell	26
2.4 A map of the median or 50 th percentile from the distribution of monthly earthquake counts within each grid cell	27
2.5 Histogram estimates of the distribution of earthquake rates for Axial Seamount and the Blanco transform	28
2.6 A time series plot of the total monthly earthquake count from the SOSUS hydroacoustic catalog	29
2.7 Earthquake time series normalized by the maximum value from each super segment showing the time dependent increase in variability across the region following the 1998 Axial eruption	30
2.8 Explorer ridge EOF modes, eigenvalues (% variance), and time series amplitudes	31
2.9 Sovanco transform EOF modes, eigenvalues (% variance), and time series amplitudes	32
2.10 Endeavour and Middle Valley Segment EOF modes, eigenvalues (% variance), and time series amplitudes	33

LIST OF FIGURES (Continued)

<u>Figure</u>	<u>Page</u>
2.11 Axial Seamount (Juan de Fuca ridge) segment EOF modes, eigenvalues (% variance), and time series amplitudes	34
2.12 Blanco transform EOF modes, eigenvalues (% variance), and time series amplitudes	35
2.13 Gorda ridge EOF modes, eigenvalues (% variance), and time series amplitudes.....	36
3.1 Map of Axial Seamount showing the locations of the ocean bottom hydrophones (OBHs; green circles), the epicentral locations and associated error of a small subset of earthquakes from 2009-2010 (red circles), the lava flows (gray) and eruptive vents (black lines) from the 2011 eruption (Caress et al., 2012), and the profile across the caldera (A-A') used for depth projections in Figure 3.4	51
3.2 Frequency and waveform displays of seismic energy recorded on the OBH array by A) a locally generated earthquake and B) an earthquake from the Western Blanco Transform Fault	52
3.3 A) The number of earthquakes detected in each swarm by the SOSUS hydrophone arrays prior to the 1998 seafloor eruption (after Dziak and Fox, 1999a)	53
3.4 Hypocentral locations and error estimates projected onto a profile across the caldera (A-A') from Figure 3.1, overlain on the <i>P</i> wave velocity model from West et al. (2001)	54

LIST OF FIGURES (Continued)

<u>Figure</u>	<u>Page</u>
3.5 A) Nearly year-long record from a bottom pressure recorder on the seafloor in the central caldera showing the preceding slow uplift and abrupt co-eruptive deflation at the time of maximum seismic energy release in 2011	55
4.1 Instrument locations and local bathymetry surrounding the YAQ-N hydrophone receiver (left), and a regional map of the Pacific Northwest coast showing the location of the study (right)	81
4.2 Spectrograms and time series showing acoustic arrivals of wave groups (a&b) from the YAQ-N mooring during a period of average wave heights $H_s = 2.74$ m	82
4.3 Spectral levels from 10-minute averages during periods of high ($H_s = 6.69$ m), average ($H_s = 2.74$ m), and low ($H_s = 0.66$ m) surf conditions	83
4.4 (a) A long-term spectrogram ($f < 100$ Hz) from the YAQ-N mooring site during the deployment year March 2010 – April 2011 emphasizes the seasonal dependence of surf-generated noise	84
4.5 (a&b) Scatter plots of octave band-averaged ($f_c = 250$ Hz, $f_c = 500$ Hz) noise levels versus wind speeds (w_s)	85
4.6 Spectrograms of vocalizations from a northeast Pacific blue whale (a), fin whale (b), and humpback whale (c) recorded by the YAQ-N receiver	86
4.7 (a) An hour-long spectrogram showing the typical frequency structure of acoustic energy radiated from a moving ship near the YAQ-N receiver	87
4.8 A summary comparison of relative acoustic energy levels associated with important sound sources recorded by the YAQ-N receiver	88

LIST OF FIGURES (Continued)

<u>Figure</u>	<u>Page</u>
4.9 Selected percentiles from the cumulative distribution of spectral energy levels recorded by the YAQ-N receiver from March 2010 – April 2011	89
4.10 (a) Average spectral levels from the present study plotted with data reported in 2 recent studies from deep water stations in the NE Pacific for comparison between deep and shallow water ambient levels	90
4.11 The 1 percentile curve from the cumulative distribution of time averaged spectral levels used to represent the noise floor for the YAQ-N receiver	91
4.12 (a) Weekly averaged SPL_{rms} calculated from 1 second data intervals for the 10-840 Hz and 5 octave bands identified by center frequencies	92

LIST OF TABLES

<u>Table</u>	<u>Page</u>
4.1 Select percentiles from the distribution of one-second root mean square sound pressure levels (SPL_{rms})	93

Submarine Earthquakes, Volcanic Eruptions and Ambient Noise in the Northeast Pacific

1 INTRODUCTION

The inherent physical properties of seawater allow for the efficient transmission of acoustic energy in the oceans. Studies ranging from basin to molecular scales and from deep to shallow water marine environments, have utilized the advantages provided by underwater propagation of acoustic signals for several decades. Underwater acoustic methods enable us to image the seafloor at a range of depths and resolutions, detect and locate seismic activity at long ranges, record and measure vocalization behavior of endangered marine mammals, and measure and assess potential impacts of anthropogenic activities on ambient noise levels for marine habitat monitoring. In the northeast Pacific Ocean the seismically active, deep water tectonic and volcanic boundaries of the Juan de Fuca plate system generate a variety of low frequency acoustic signals providing information for both regional and localized geophysical studies. Moving in to the shallower waters of the North American continental shelf, a clear need for acoustic monitoring has emerged given the rising noise levels expected to accompany industrial and commercial marine energy development along the coast. These studies display a range of acoustic applications and derived products whose information are used to examine a variety of scientific issues throughout the northeast Pacific.

Chapter 2 of this dissertation, entitled “Mid-ocean ridge and transform earthquake variability in the northeast Pacific” quantifies space/time patterns in seismicity from a

regional, acoustically derived earthquake catalog using sound channel, bottom mounted hydrophone arrays. Tertiary (T -) waves of seafloor earthquakes are seismically generated acoustic waves that travel long distances through the ocean sound channel (Tolstoy and Ewing, 1950). The *SOFAR* (*SOund Fixing And Ranging*) channel, a temperature and depth dependent low acoustic velocity zone, acts as a wave guide allowing low frequency acoustic energy to propagate long distances (~ 1000 km) with little attenuation loss. An ideal combination of pressure, temperature and salinity in the open seas typically places the *SOFAR* channel axis at ~ 1000 m depth. Acoustic methods applied to T - waves recorded in the northeast Pacific has generated a regional catalog of earthquakes ($m_b > 2.5$) with detection capabilities 1.5 – 2 orders of magnitude more sensitive than land based seismic networks (Dziak et al., 2011). Chapter 2 of this dissertation examines the temporal and spatial distribution of T - phase derived earthquake epicenters along the plate boundaries of the northeast Pacific through first order statistics and empirical orthogonal function (EOF) analysis.

Analysis from the remotely derived acoustic earthquake catalog in Chapter 2 quantifies a well documented, anomalous seismic event associated with the ascending and down-rift propagation of a magmatic dike intrusion and eruption at Axial Seamount in 1998 (Dziak and Fox, 1999b). Zooming in from the regional scale investigation of Chapter 2, Chapter 3 entitled, “Seismic cycles, seafloor deformation and volcanic eruptions at Axial Seamount, Juan de Fuca ridge” uses acoustic signals from a local array of ocean bottom hydrophones (OBH) to characterize the micro-seismicity leading up to a subsequent intrusion and eruption at Axial in 2011. Locally generated earthquake signals were acoustically identified from a unique

spectral signature composed of a series of sea surface reflections separated by the water depth travel times. A time series of OBH derived micro-earthquakes in and around the Axial Seamount edifice is compared with previous, regionally detected earthquake rates prior to the event in 1998 (Dziak and Fox, 1999a) as well as seafloor deformation measurements made on the caldera floor (Chadwick et al., 2012).

The focus of the next study moves east from the Juan de Fuca Ridge into the shallow continental shelf waters of the Pacific Northwest off the coast of Oregon. Chapter 4 entitled, “Observations of shallow water marine ambient sound: the low frequency soundscape of the central Oregon coast” examines the first long-term (1 year) continuous time series of shallow water ambient noise levels recorded in the region. This study investigates the temporal contribution of natural and anthropogenic sound sources to shallow water ambient noise variability. Spectral characterizations and correlations with independent measurements of environmental conditions and anthropogenic activity (e.g. fishing traffic) provide a strong basis for development of a low frequency sound budget for the area. Results from this research provide important baseline information for future coastal industrial and commercial energy development.

1.1 REFERENCES

Chadwick Jr, W. W., Nooner, S. L., Butterfield, D. A., and Lilley, M. D., 2012, Seafloor deformation and forecasts of the April 2011 eruption at Axial Seamount: *Nature Geoscience*, v. 5, no. 7, p. 474-477.

- Dziak, R. P., and Fox, C. G., 1999a, Long-term seismicity and ground deformation at Axial Volcano, Juan de Fuca Ridge: *Geophysical Research Letters*, v. 26, no. 24, p. 3641-3644.
- , 1999b, The January 1998 earthquake swarm at Axial Volcano, Juan de Fuca Ridge: Hydroacoustic evidence of seafloor volcanic activity: *Geophysical Research Letters*, v. 26, no. 23, p. 3429-3432.
- Dziak, R. P., Hammond, S. R., and Fox, C. G., 2011, A 20-year hydroacoustic time series of seismic and volcanic events in the Northeast Pacific Ocean: *Oceanography-Oceanography Society*, v. 24, no. 3, p. 280.
- Tolstoy, I., and Ewing, M., 1950, The T phase of shallow-focus earthquakes: *Bulletin of the Seismological Society of America*, v. 40, no. 1, p. 25.

**2 MID-OCEAN RIDGE AND TRANSFORM EARTHQUAKE VARIABILITY
IN THE NORTHEAST PACIFIC**

Joseph H. Haxel and Robert P. Dziak

To be submitted to *Geochemistry, Geophysics, Geosystems*

2.1 ABSTRACT

Since August 1991 U.S. Navy hydrophones (SOSUS) have been used by the National Oceanic and Atmospheric Administration (NOAA) and Oregon State University to monitor seismicity along the submarine tectonic plate boundaries in the northeast Pacific Ocean. Epicenters for more than 20,000 earthquakes from 1991-2002 epicenters have been localized using the hydroacoustic Tertiary (*T*-) phase generated during seafloor seismic events. First order analyses, including mean, skewness and median maps, show the decadal scale background patterns of seismic activity across the region and suggest a fundamental difference in the temporal distribution of seismicity between mid ocean ridge segments and oceanic transforms at intermediate spreading rates. The earthquake catalog is further organized into geologic super segments revealing the Blanco transform as the most seismically active feature in the northeast Pacific. Empirical orthogonal function (EOF) analyses is applied to each super segment in order to decompose time/space earthquake patterns and quantify variability in the context of background levels. The long-term time averaged monthly rates of seismicity show a substantial increase in earthquakes beginning in 1998, peaking in late 2000 and returning to background levels during 2001. This increase in earthquake rates is observed in varying levels across all of the seismically active submarine plate boundary features suggesting a short-term plate scale change in seismic energy.

2.2 INTRODUCTION

The remote location of earthquake-generating submarine tectonic and volcanic features in the northeast Pacific results in limited spatial coverage provided by land based seismic networks. Meanwhile, hydroacoustic methods used in seafloor earthquake studies have shown improvements in energy based detection levels of catalog completeness on the order of 1.5 - 2.0 orders of magnitude greater sensitivity than those derived from land based stations (Bohnenstiehl et al., 2002). Over the last two decades, restricted access to acoustic data from the U.S. Navy's Sound Surveillance System (SOSUS) of military hydrophone arrays in the northeast Pacific has enabled the NOAA/ Pacific Marine Environmental Laboratory and Oregon State University Acoustics Program to construct a unique catalog of seismic events along the Juan de Fuca (JdF) and Gorda plate systems (Dziak et al., 2011). From remotely capturing the seismic details of mid-ocean ridge volcanic eruptions and dike intrusion along the intermediate spreading (~ 6 cm/yr) JdF and Gorda ridges (Bohnenstiehl et al., 2004a; Dziak and Fox, 1999; Dziak et al., 1995; Fox and Dziak, 1998; Fox et al., 1995) to research focused on mid-plate and oceanic transform tectonic processes ((Cronin and Sverdrup, 2003; Dziak, 2001; Dziak et al., 2003; Fox and Dziak, 1999), the SOSUS, acoustically derived seismic catalog has provided a detailed perspective not afforded by land base seismic networks alone.

The purpose of this paper is to identify and quantify fundamental spatial and temporal patterns of seismic activity along the submarine plate boundaries of the northeast Pacific at a completeness level of $m_b > 2.5$ (Bohnenstiehl et al., 2002) using a decade of earthquakes from the SOSUS catalog. From first order mean, median and

skewness statistics we gain important basic information on where and how often earthquakes occur and how characteristic variability may be linked with the volcano-tectonic structures of the plate system. Furthermore, eigenfunction analysis, a linear decomposition technique for complex systems traditionally used in oceanographic and atmospheric research (Preisendorfer and Mobley, 1988) and more recently applied to identify, quantify and forecast seismicity pattern dynamics in historical and simulated earthquake catalogs (Goltz, 2001; Holliday et al., 2007; Rundle et al., 2000; Tiampo et al., 2002), is applied to the SOSUS data at both regional and geologic segment scales. The eigenfunction technique applied here is used to objectively identify a unique set of seismicity patterns and to quantify their importance in terms of the observed variability within the earthquake catalog.

2.3 DATA

The SOSUS earthquake catalog, composed of hydrophone recorded *T*-phase seismicity from the northeast Pacific, provides the primary dataset in this analysis. Estimates for the location (latitude and longitude) and origin time of a given earthquake are calculated by an iterative algorithm that seeks to minimize the difference between the predicted and observed *T*-phase arrival time at fixed hydrophone locations (Fox et al., 2001b). Modeled propagation of *T*-phases is carried out with standard models of ocean sound speeds (Teague et al., 1990). To avoid gaps in the catalog resulting from intermittent outage periods where particular hydrophone arrays were offline (Dziak et al., 2011), this analysis is focused on data spanning September 1991 – January 2002 for a total of 21,934 seismic events in the northeast

Pacific (Fig. 2.1). Given the improved detection capability afforded by efficient acoustic propagation of *T*-phase energy in the sound channel (Tolstoy and Ewing, 1950) and the good azimuthal station coverage of the SOSUS arrays in relation to the spreading ridges and tectonic features of the northeast Pacific (Dziak et al., 1996) the SOSUS catalog provides a more complete representation of seismic energy release than land based networks. Model estimates based on the geometry of the hydrophone arrays and a normally distributed 0.5 second timing error in the *T*-phase arrival pick show epicentral location error along the ridges and transforms range from 0.5 - 3.5 km in latitude and 0.8 - 2 km longitude at the 68% confidence interval (Dziak et al., 2011). As a quality control measure, earthquakes for ridge and transform segments with location errors larger than the mean plus standard deviation of the distribution in location error are removed from this analysis.

Seismicity is binned using isotropic length scales of 10 minutes in latitude and longitude forming discrete spatial units ~ 18 km to a side. This conservative spatial scaling is suitable for the resolution of interest in this analysis and a factor of five larger than estimates of epicentral error location. A time series of earthquake occurrence is constructed for each bin location by summing the total earthquakes counted during a 1-month interval for a total of $N = 125$ time steps at $M = 439$ spatial bins. Bins containing < 5 earthquakes over the 10 year record length are removed from the analysis. The combination of monthly earthquake rate time series at each bin location forms the parameter basis for the space-time pattern analysis.

2.4 BASIC EARTHQUAKE PATTERNS

2.4.1 *Ridges versus transform earthquakes*

First order statistics including sample mean, skewness and median values taken from the distribution of observations during the 10-year period at each grid cell provide valuable information on the spatial structure and general time dependent behavior of seismicity along the plate boundaries. A map of the mean statistic (μ) in units of earthquakes/month reveals the spatial structure of zones where the total number of observed earthquakes is high (Fig. 2.2). Axial Seamount, the Endeavor segment, Middle Valley segment and the western Blanco Transform show elevated levels of mean seismicity rates compared with surrounding areas. Because the mean statistic is influenced by large events where the number of located earthquakes within a month can reach in to the tens of thousands (e.g. Axial Seamount eruption), the map of mean values better represents where concentrated earthquake activity occurs rather than background seismicity rates.

A similar map of the skewness statistic (γ) calculated as the third standardized moment from the distribution of observed earthquake rates at each grid cell (Fig. 2.3) shows high levels of positive skewness localized around Axial and the Endeavour and Middle Valley ridge segments. Positive skewness implies the large majority of monthly observations of earthquake occurrence in these highly skewed regions lie well below the mean earthquake rates shown in Figure 2.2. The combination of elevated mean seismicity rates accompanied by strongly positive skewness at Axial and the Endeavour and Middle Valley ridge segments, indicates variability within these segments occurs as intense, impulsive changes in seismicity rates resulting from

large, brief seismic events associated with magmatic dike intrusions. Meanwhile, the area of the western Blanco transform that exhibits similar elevated levels of mean seismicity (Fig. 2.2) lacks a corresponding highly positive area of skewness observed at the Axial, Endeavour and Middle Valley regions (Fig. 2.3). Therefore, the lower skewness levels suggest mean earthquake rates for the Blanco transform may represent steady state or background levels of seismicity.

Although volcanic and spreading ridge features exhibit highly positive skewness implying background seismicity rates are not well described by simple time-averaged mean values, the median or 50th percentile statistic provides a better representation of background earthquake rates. A map of the median values from the distribution of seismicity rates at each grid cell shows the Blanco transform as the most consistent seismically active geologic feature in the northeast Pacific (Fig. 2.4) with rates ranging from 1-2 earthquakes per month along the fault zone. In contrast, the volcanically influenced ridge segments (Axial, Endeavour, Middle Valley) display long periods of quiescence with median background rates of zero interrupted by intense episodic bursts in seismic energy release accompanying rising magmatic dikes. The lower skewness and higher median values observed along the Blanco suggest more steady tectonic earthquake rate behavior accommodating slip along the transform in response to motion of the Juan de Fuca and Pacific plates. This fundamental difference in earthquake behavior between mid-ocean ridge and transform segments in the northeast Pacific is readily observed in a histogram plot of the observed distribution of earthquake rates spatially integrated over the length of the Axial and Blanco segments in Figure 2.5. A single 1500 event/month value associated

with the 1998 volcanic eruption at Axial is not shown off the right side of the scale in the lower panel in order to emphasize smaller scale variability prior to the eruption. The Blanco transform earthquakes are more normally distributed through time than seismicity from Axial further supporting the basic temporal difference in earthquakes generated in ridge and oceanic transform settings.

2.4.2 Time dependent regional earthquake rate changes

A monthly time series of total seismicity from the spatially binned northeast Pacific SOSUS earthquake catalog is shown in Figure 2.6. A general increase in seismic activity levels is observed, beginning with the dike intrusion and eruption at Axial Seamount in 1998, continuing through mid-2001 and then trending downward to the end of the record. In order to examine the spatial character of this increase in seismicity, the record was organized into six super segments from north to south: Explorer ridge (Expl), Sovanco transform (Svnc), Endeavour ridge (Endv), the rest of the Juan de Fuca (JdF), Blanco transform (Blnc), and the Gorda ridge (Gord). A monthly time series was constructed for each super segment and normalized by its maximum value to show long-term variability at the super segment scale (Fig. 2.7). Subsequent to the 1998 eruption, super segments north of Axial Seamount display increased variability through mid-2001 mostly as brief, intense rate changes occurring more frequently. Whereas, segments south of Axial Seamount exhibit a more gradual rise in seismic activity levels raising background levels. This three year increase in earthquake variability observed along all of the bounding segments of the plate

system suggests the 1998 Axial dike intrusion and eruption may have triggered a plate scale change in seismic energy release.

2.5 EMPIRICAL ORTHOGONAL FUNCTION (EOF) ANALYSIS

2.5.1 Eigenfunction Methods

Empirical Orthogonal Function (EOF) analysis is a linear decomposition technique using eigenfunctions to describe complexity in large datasets as orthonormal patterns of variability. EOF analysis has been successfully used in oceanographic and atmospheric research over the last couple of decades (Preisendorfer and Mobley, 1988). While most other orthogonal function representations are defined prior to the transformation of the data (e.g. principle components analysis), the particular set of orthogonal functions (EOFs) described here is derived empirically from the statistics of the binned data matrix. A covariance EOF approach is used, alternative to the correlation method (normalizing each time series to unit variance), in order to preserve the true earthquake rate amplitudes and deviations from the background sample mean at each grid location.

The EOF approach described here decomposes the space/time variability of the earthquake catalog into a set of uncorrelated, orthonormal modes or eigenvectors, their associated time series or factor loadings, and their corresponding eigenvalues. The eigenvectors characterize the spatial pattern and relative amplitudes between grid cells associated with each mode, the time series of each eigenvector mode describes its temporal dependency, and the eigenvalues quantify the relative importance of each mode of variability in describing the dataset. Although there is no requirement for

uniform spatial sampling, a critical component of EOF analysis in this application is that the grid locations remain fixed in space. By removing the time averaged earthquake rate (eq.2.1) from each x_m , ($m = 1, \dots, M$) grid cell location at each time interval t_n , ($n = 1, \dots, N$) prior to the EOF transformation, calculated eigenvector modes represent variability around mean values at each grid cell.

$$q_m(t_n) = x_m(t_n) - (\sum_{n=1}^N x_m(t_n))/N \quad (2.1)$$

The set of mean-removed time series' $q_m(t_n)$, consists of $m = 1, \dots, M$ grid cell locations each with observation time steps t_n , $n = 1, \dots, N$. This set of time series' $q_m(t_n)$ can be organized into an $N \times M$ matrix \mathbf{D} (eq.2.2) composed of N rows of observations at M different grid cell locations.

$$\mathbf{D} = \begin{bmatrix} q_1^1 & \dots & q_1^M \\ \vdots & \ddots & \vdots \\ q_N^1 & \dots & q_N^M \end{bmatrix} \quad (2.2)$$

\mathbf{D} is therefore an $N \times M$ matrix of real values corresponding to the number of earthquakes (minus the mean) within a spatial grid location (m) that occur during a monthly time period (n). The covariance matrix \mathbf{C} of the earthquake time series' matrix \mathbf{D} is calculated by multiplying \mathbf{D} by its transpose \mathbf{D}^T (eq.2.3).

$$\mathbf{C} = \mathbf{D}^T \mathbf{D} \quad (2.3)$$

C is therefore an $M \times M$ real symmetric matrix of mean cross products between the M time series' of \mathbf{D} (eq.2.4).

$$\mathbf{C} = \begin{bmatrix} \{q_1^2\} & \cdots & \{q_1 q_M\} \\ \vdots & \ddots & \vdots \\ \{q_M q_1\} & \cdots & \{q_M^2\} \end{bmatrix} \quad (2.4)$$

The diagonal elements of C are the sample variances at the M grid locations and the off diagonal elements are the sample cross covariance between the different grid locations. The eigen-structure of the covariance matrix C is calculated using standard computational techniques (MATLAB® 7.12, The Mathworks Inc., Natick, MA, 2011) to produce the orthogonal set of eigenvectors E and associated eigenvalues V where both E and V satisfy the equation for the matrix eigenvalue problem (eq.2.5).

$$\mathbf{C} \mathbf{E}_k = \mathbf{V}_k \mathbf{I} \mathbf{E}_k \quad (2.5)$$

C is the $M \times M$ real, symmetric mean product matrix described by equation 2.4, I is the $M \times M$ identity matrix, \mathbf{E}_k is the $M \times 1$ vector consisting of the k^{th} column of the $M \times M$ matrix E of orthogonal functions and \mathbf{V}_k is the associated eigenvalue.

Each eigenvector from E represents a spatial pattern or “mode” of uncorrelated earthquake variability within time series data matrix D. The relative importance of a particular EOF mode $p(k)$ over the time interval of the data set is quantified by taking the ratio of the eigenvalue for that mode against the sum of all M eigenvalues (eq.2.6).

$$p(k) = \frac{V_k}{\sum_{i=1}^M V_i} \quad (2.6)$$

Accordingly, the first mode or eigenvector axis points in the direction of maximum variance defined by the first eigenvalue $p(1)$, the second eigenvector in the direction of the second largest amount of variance $p(2)$ and so on. The orthonormal time series history $B(k)$ for each EOF mode of variance is resolved by projecting the initial data matrix D ($N \times M$) onto the basis eigenvector matrix E ($M \times M$) (eq2.7).

$$B = D E \quad (2.7)$$

This yields the ($N \times M$) matrix B consisting of N rows of time dependent expansion coefficients corresponding to M independent EOF spatial modes. Therefore, the contribution of the k^{th} EOF mode at an instant in time t_i is realized by multiplying the amplitude scalar $B_k(t_i)$ with eigenvector E_k .

Generally, the first few EOF modes describe a large majority of the observed variance within dynamical systems (Preisendorfer and Mobley, 1988). This eigenfunction based decomposition technique applied to the northeast Pacific SOSUS earthquake catalog provides an objective method for quantifying spatial modes of earthquake rate changes and their time dependent nature over a decadal time scale.

2.5.2 Regional EOF earthquake patterns

Dziak et al., (2011) present results from a regional scale EOF analysis of the northeast Pacific SOSUS *T*-phase epicenters where 4 distinct eigenfunctions or modes of variability account for up to 99% of the variance observed in the catalog. The first EOF mode (65.6% of variance) is associated with the January 1998 eruption of Axial Seamount, (Dziak and Fox, 1999), the second EOF mode (10.5% of variance) shows the change in seismicity rate due to the Endeavour segment swarms in June 1999 and January 2000 (Bohnenstiehl et al., 2004b), the third mode (7.8% of variance) resolves the seismic activity increase observed along the Heck Seamount chain in early 1992 (Dziak, 2006), and the fourth mode (6.7% of variance) describes the spatial and temporal pattern of seismicity rate change associated with the Middle Valley ridge segment earthquake swarm (Davis et al., 2004). Each of these EOF modes from the analysis presented by (Dziak et al., 2011) occur along ridge segments and can be readily identified within the mean and skewness maps (Figs. 2.2 & 2.3) presented in section 2.4.1. The high amount of variance explained by the first regional EOF mode (eigenvalue = 65%) indicates the 1998 dike intrusion and eruption at Axial Seamount was the largest earthquake rate increase within the Juan de Fuca plate system over a decadal time scale (1991-2002).

2.5.3 Segment scale EOF earthquake patterns

The regional EOF analysis of (Dziak et al., 2011) primarily describes the short intense bursts in seismic activity observed during dike intrusion events along segments of the spreading ridges. These temporally skewed events produce thousands

of earthquakes within a short period and therefore dominate the mean removed variability of the earthquake catalog. In order to identify and quantify patterns in space/time variability along other seismically active, but more normally distributed plate boundary segments (e.g. Blanco transform), the EOF method is applied to the spatially isolated time series of grid cells within each super segment. In order to reconstruct the observed number of earthquakes in the SOSUS catalog described by a particular EOF mode of variability at any instant in time, multiply the time series amplitude value for that period $B_k(t_i)$ by the spatial EOF map E_k and add in the sample mean value for each grid cell (i.e. Fig. 2.2).

Moving from north to south along the plate boundaries, the Explorer ridge earthquake time series is mostly described by two distinct EOF modes with eigenvalues accountable for 63% (EOF1) and 19% (EOF2) for a total of 82% of the total mean removed earthquake rate variability observed along this ridge segment (Fig. 2.8). The mode 1 pattern is focused on the southern Explorer ridge showing pulses of increased seismic activity in 1992, 1998, and 2000. The second mode or pattern is located on the southern end of the Dellwood Seamounts, marking a significantly smaller earthquake rate change occurring in the first half of 1992.

EOF analysis of the Sovanco transform to the south of the Explorer ridge also produces 2 distinct EOF modes with eigenvalues 29% (EOF1) and 18% (EOF2) combining for 47% of the total variance observed (Fig. 2.9). Notice the increase in seismic activity illustrated by rising levels of variability starting around the time of the 1998 eruption at Axial Seamount and punctuated by peaks in 1999 (EOF1) and early 2001 (EOF2) both located on the eastern end of the transform region.

Eigenfunction analysis of the seismically active ridge segments found directly below the Sovanco transform produces 3 significant EOF modes with eigenvalues 45% EOF1, 37% EOF2, and 7% EOF3 combining for a total of 89% of the variance in the record (Fig. 2.10). The modes from this analysis mimic the second through fourth EOFs from regional analysis (Dziak et al., 2011) corresponding to the 1992 Heck Seamount earthquake swarm (EOF1(Dziak, 2006)), the 1999 and 2000 Endeavour ridge segment events (EOF2(Bohnenstiehl et al., 2004b)), and the 2001 Middle Valley ridge segment intrusion (EOF3(Davis et al., 2004)). Each of these EOF modes shows little variability outside of the sharp brief rise associated with each particular seismic event indicating limited background seismicity within the region.

The ridge segment surrounding Axial Seamount generates a single EOF mode with an eigenvalue describing 99% of the variance along the segment (Fig. 2.11). The spatial pattern and temporal signature of the EOF describe the seismicity generated by the anomalous 1998 dike intrusion and eruption at Axial Seamount (Dziak and Fox, 1999). Outside of the seismicity associated with this event, EOF analysis shows no significant background patterns or recurrence of earthquakes along any section of this segment.

Blanco transform EOF analysis generates four significant modes of variability with eigenvalues 23% EOF1, 13% EOF2, 11% EOF3, 10% EOF4 accounting for 67% of the variance in the time series (Fig. 2.12). The small differences in eigenvalues results from modest deviations from background seismicity levels along the Blanco transform. In contrast to the EOF modes associated with spreading ridge segments, the earthquake swarms along the Blanco are typically not so large in number that they

tend to dominate the observed variance in the time series. Spatial and temporal patterns from the four modes suggest the western Blanco is the region along the transform most influenced by brief intense periods of seismic activity above background levels. This result coupled with significantly larger mean and median (Figs. 2.2 & 2.4) earthquake rates suggest the western portion of the Blanco transform is the most seismically active plate boundary found in the northeast Pacific (Braunmiller and Nábělek, 2008). Additionally, a significant change in the variability of the EOF time series amplitudes is observed after the 1998 eruption at Axial Seamount associated with the increase in background seismicity levels discussed in section 2.4.2.

Along the Gorda ridge segment, two EOF modes with eigenvalues 33% EOF1 and 17% EOF2 combine to describe 50% of the observed variance in earthquake rate variability (Fig. 2.13). The first EOF mode describes seismicity associated with a seafloor spreading episode on the central Gorda Ridge (Fox et al., 2001a) and EOF mode 2 describes the 1996 and 1997 volcanic activity observed and located by the SOSUS arrays on the northern Gorda Ridge (Fox and Dziak, 1998). The EOF generated patterns of seismicity along the Gorda ridge are controlled by short, intense bursts of seismic energy release related to intrusive magmatic events that are also common to the other spreading ridge segments of the Juan de Fuca system in this analysis.

2.6 DISCUSSION

Patterns of earthquake variability in time and space are not easily recognized and often difficult to quantify with traditional clustering algorithms (e.g. single link clustering). Furthermore, these techniques often require subjective parameterization for identifying related events within the catalog (Frohlich and Davis, 1990). Here we have shown the successful application of eigenfunction methods to both identify and more importantly quantify patterns in time and space of earthquake rate variability within the context of mid-ocean ridge and transform boundary segments of the Juan de Fuca plate system. The EOFs represent uncorrelated modes of variability described by the statistics of the covariance matrix of observations not requiring any particular subjective parameterization outside of the desired spatial and temporal resolution of the analysis (i.e. grid spacing, time step). Furthermore, the variance explained by an EOF mode is defined by its eigenvalue, providing a quantitative comparison of that particular pattern of earthquake rate change against the other modes of variability. Similarly, the time series amplitude of the EOF modes provides the temporal signature of the spatial earthquake patterns, identifying recurrence intervals and where in time within the data set particular modes found.

The first order statistics and EOF decomposition shown here reveal some fundamental differences between seismicity observed at intermediate spreading rate mid-ocean ridges and transforms. Maps of the sample mean, skewness and median statistics illustrate the contrasting temporal distribution in earthquake rates. Ridge segments exhibit high mean values, are highly skewed by episodic magmatic intrusions, and have median values around zero attributed to limited background

seismicity. Meanwhile, transforms may also have high mean values, but differ from the ridges with lower skewness and higher medians indicative of higher background earthquake rates. This difference is also reflected in the eigenvalues and time series amplitudes of the EOF analysis. Ridge based EOFs trend toward higher eigenvalues where the amount of variance explained by the modes is wrapped into brief, intense bursts of seismic energy release experienced during magmatic dike intrusions. Outside of these intrusion events, the background earthquake rates are minimal. In contrast, the transform EOFs display more time dependent variability in their amplitude time series and are often associated with smaller eigenvalues.

The increase in seismic energy observed along all of the bounding segments from 1998-2001 has implications for a change in plate scale dynamics during that period. Additionally, the decadal time scale intrusion and eruption at Axial Seamount in 1998 (which dominates the SOSUS catalog (Dziak et al., 2011)) provides further support of a plate scale increase in seismicity. Unfortunately, outages and the degradation of the SOSUS hydrophone arrays over the last decade have significantly reduced the earthquake localization capabilities of the system limiting time series comparisons after that period.

2.7 CONCLUSIONS

The more sensitive earthquake detection capability provided by the U.S. Navy's hydroacoustic (SOSUS) arrays affords an improved understanding of earthquake activity along the submarine plate boundaries of the northeast Pacific. First order statistics show a fundamental difference in the temporal distribution of seismicity

between spreading ridge segments and transform fault zones. Ridge seismicity is characterized by a lack of background seismicity episodically interrupted with brief, intense swarms of earthquakes associated with magmatic intrusion events. While transform fault zones exhibit more steady levels of background earthquake activity. Empirical orthogonal function (EOF) decompositions of time/space variability are used to identify and quantify patterns of earthquake rate changes along each super segment. Additionally, EOF eigenvalues and time series amplitudes show characteristics particular to spreading ridge and transform settings. Interestingly, a three-year plate scale increase in seismic activity is observed commencing with the large magmatic dike intrusion event at Axial Seamount in 1998.

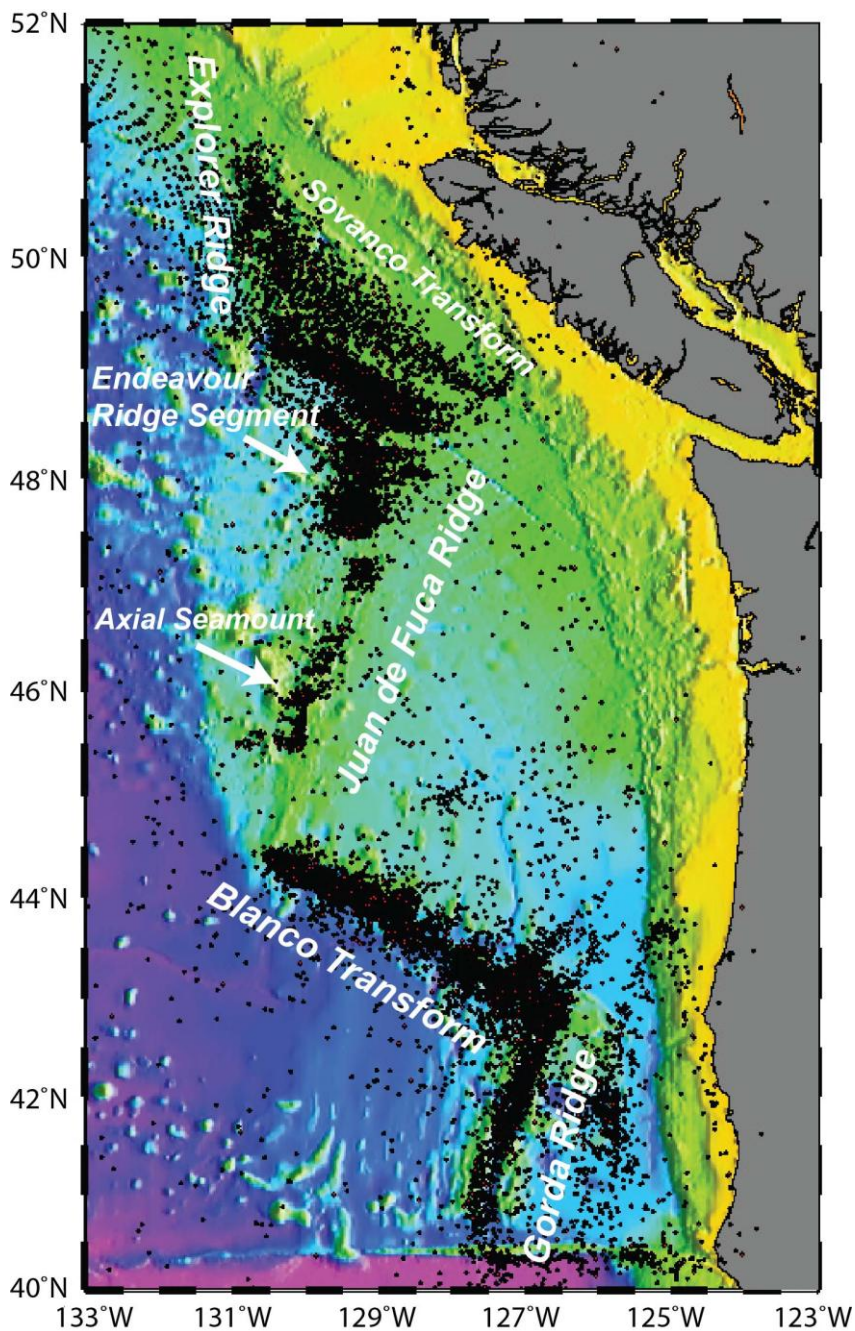


Figure 2.1 A decade of *T*-phase derived epicenters from the SOSUS hydroacoustic catalog spanning the period from September 1991 - January 2002. A total of 21,934 localized seismic events outline the ridge and transform boundaries of the Juan de Fuca and Gorda systems in the northeast Pacific Ocean.

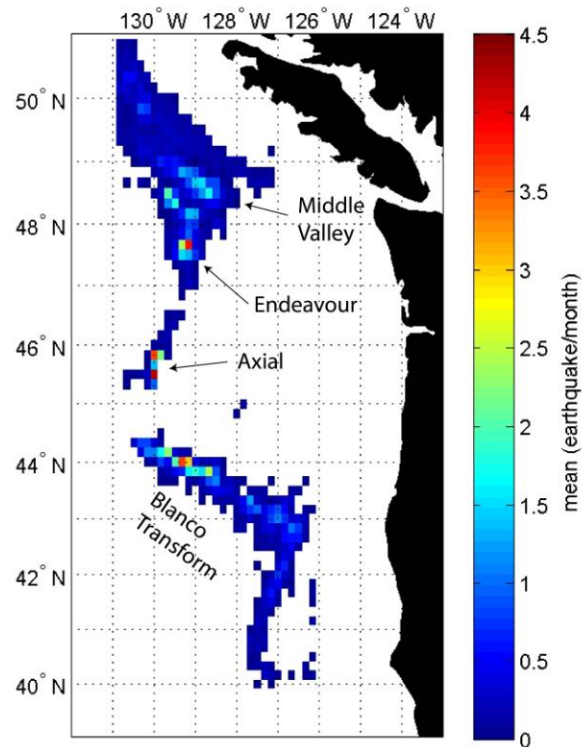


Figure 2.2 A map of the time averaged mean value of earthquakes per month in each spatially binned ($10' \times 10'$) area from the SOSUS earthquake catalog (1991-2002).

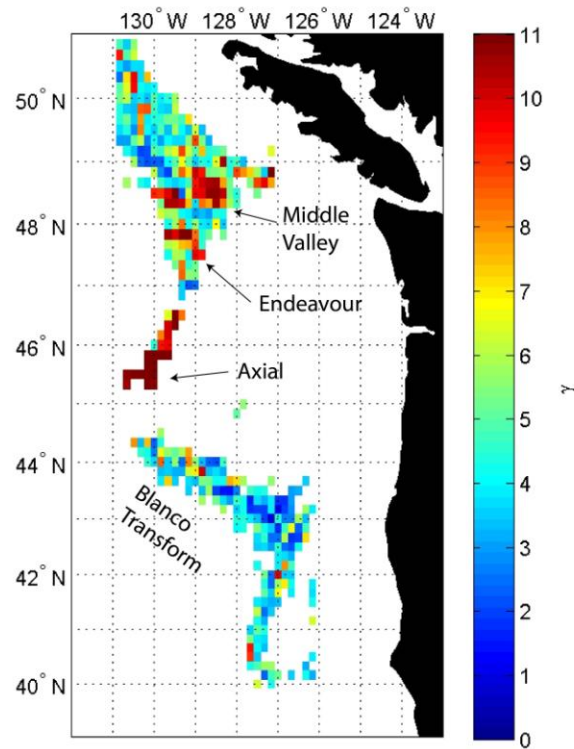


Figure 2.3 A map of skewness from the distribution of monthly earthquake counts within each grid cell.

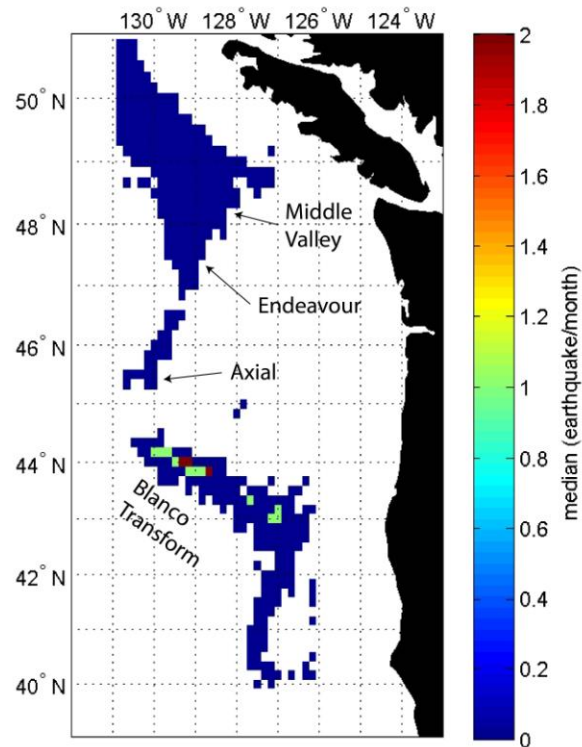


Figure 2.4 A map of the median or 50th percentile from the distribution of monthly earthquake counts within each grid cell.

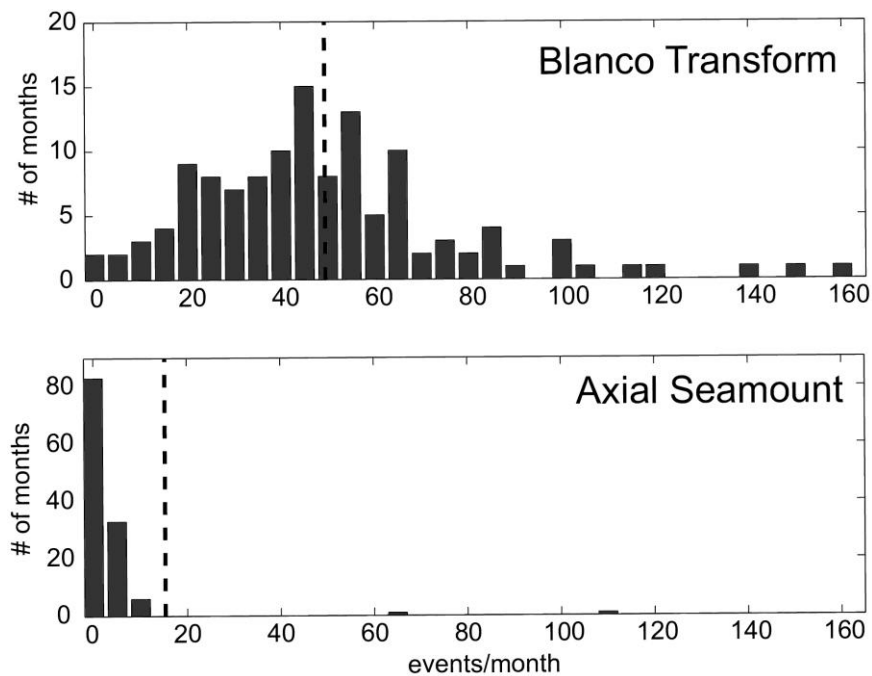


Figure 2.5 Histogram estimates of the distribution of earthquake rates for Axial Seamount and the Blanco transform. One 1500 event/month outlier value is not shown off the right scale of the lower Axial Seamount plot. Mean values are shown with dashed lines.

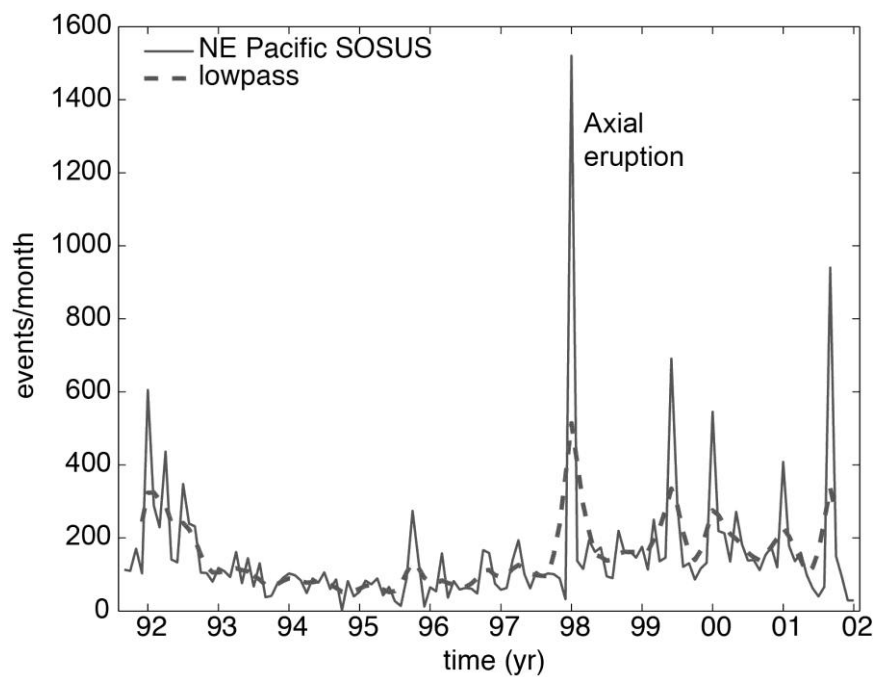


Figure 2.6 A time series plot of the total monthly earthquake count from the SOSUS hydroacoustic catalog. A low pass filter was applied to the time series generating the dashed line to emphasize the rise in overall seismicity following the 1998 eruption at Axial Seamount.

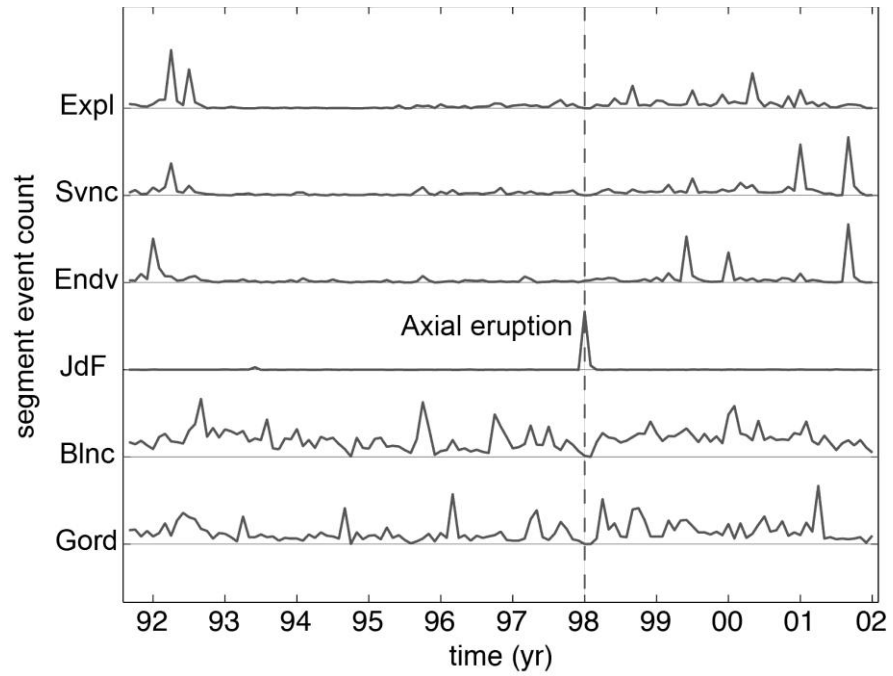


Figure 2.7 Earthquake time series normalized by the maximum value from each super segment showing the time dependent increase in variability across the region following the 1998 Axial eruption.

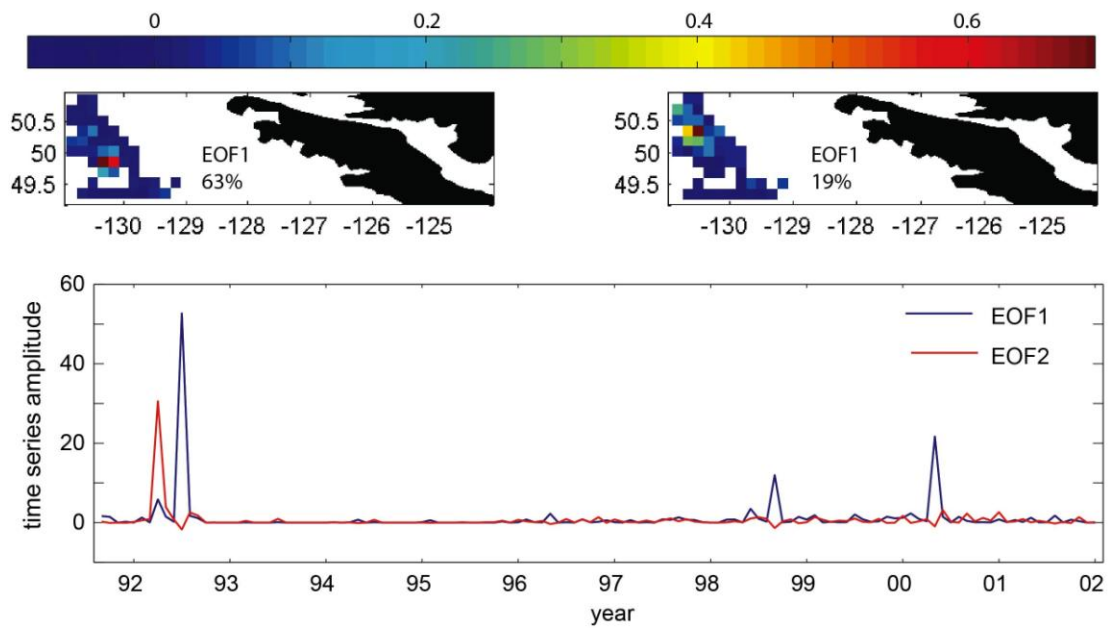


Figure 2.8 Explorer ridge EOF modes, eigenvalues (% variance), and time series amplitudes.

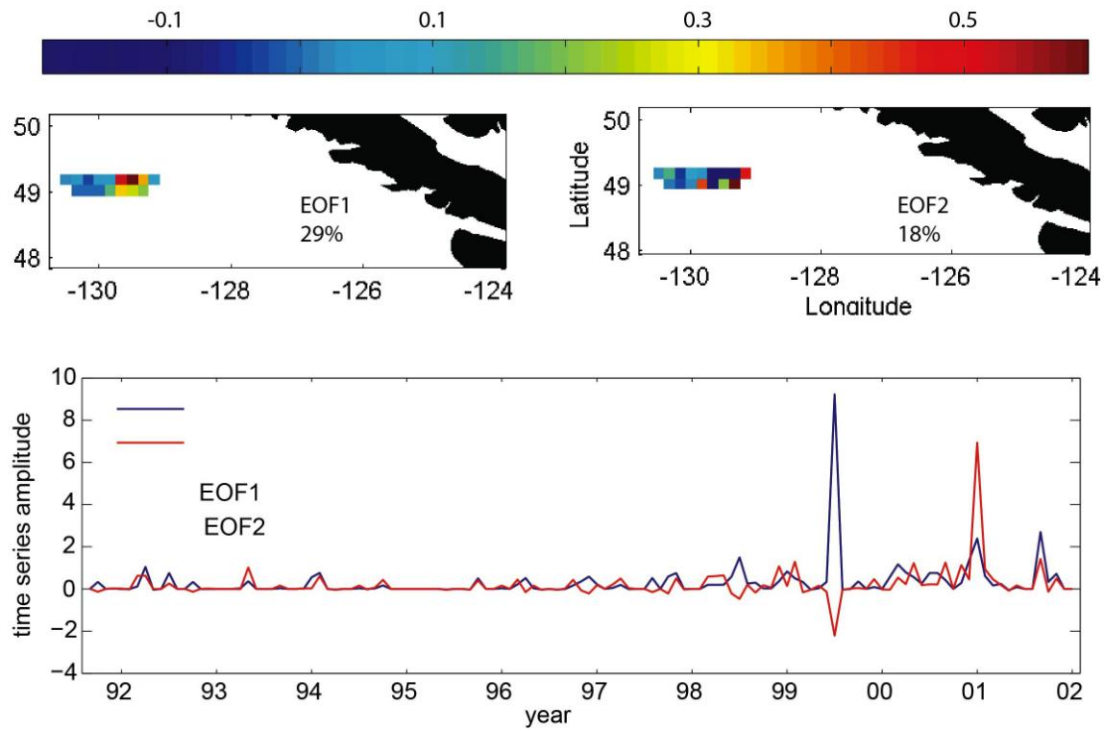


Figure 2.9 Sovanco transform EOF modes, eigenvalues (% variance), and time series amplitudes.

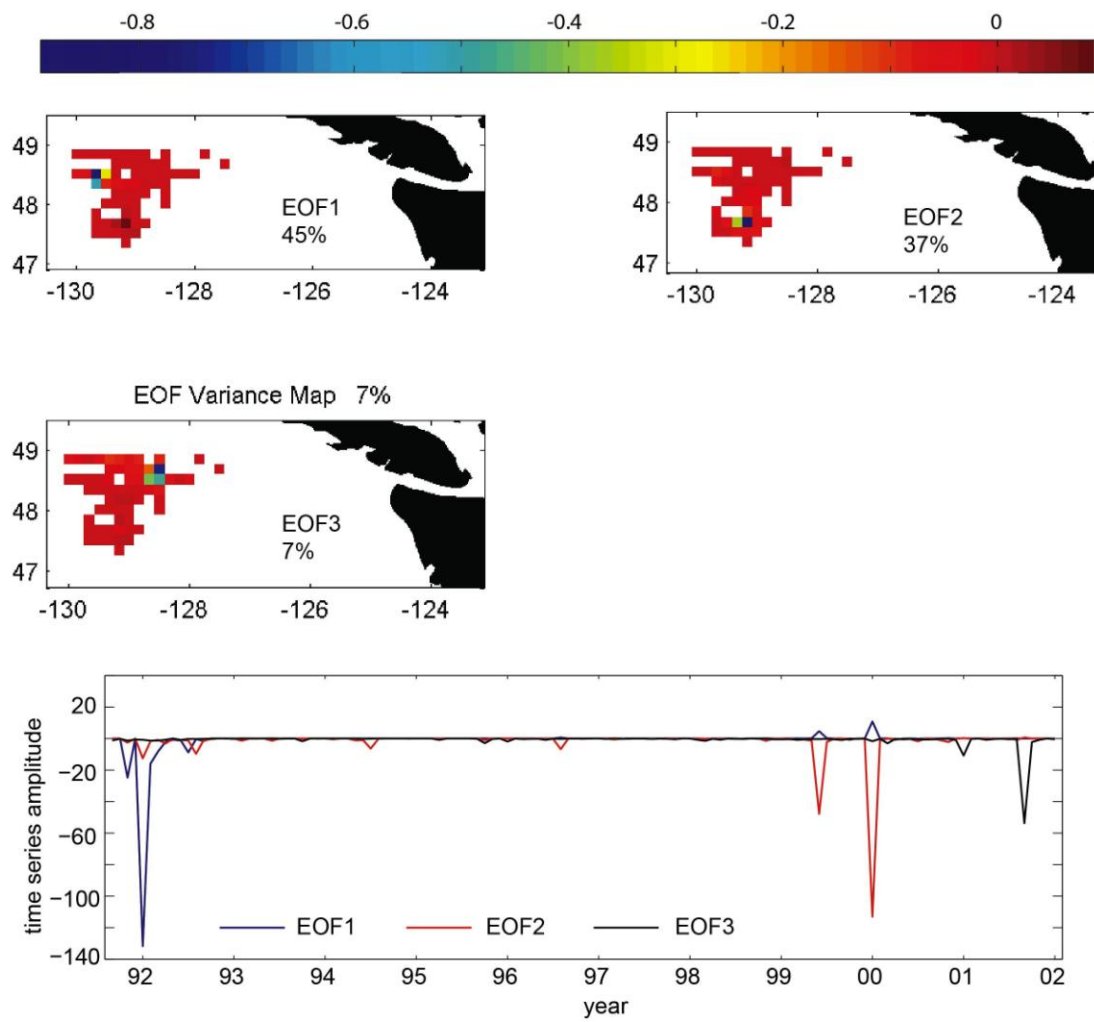


Figure 2.10 Endeavour and Middle Valley Segment EOF modes, eigenvalues (% variance), and time series amplitudes.

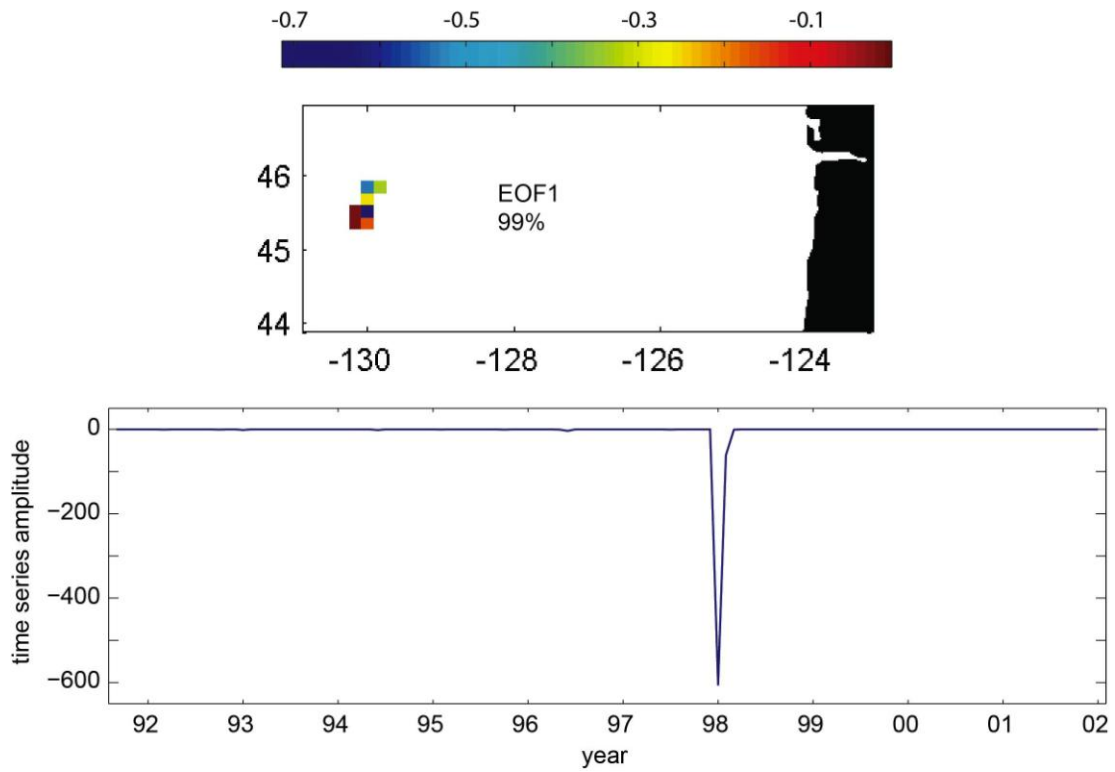


Figure 2.11 Axial Seamount (Juan de Fuca ridge) segment EOF modes, eigenvalues (% variance), and time series amplitudes.

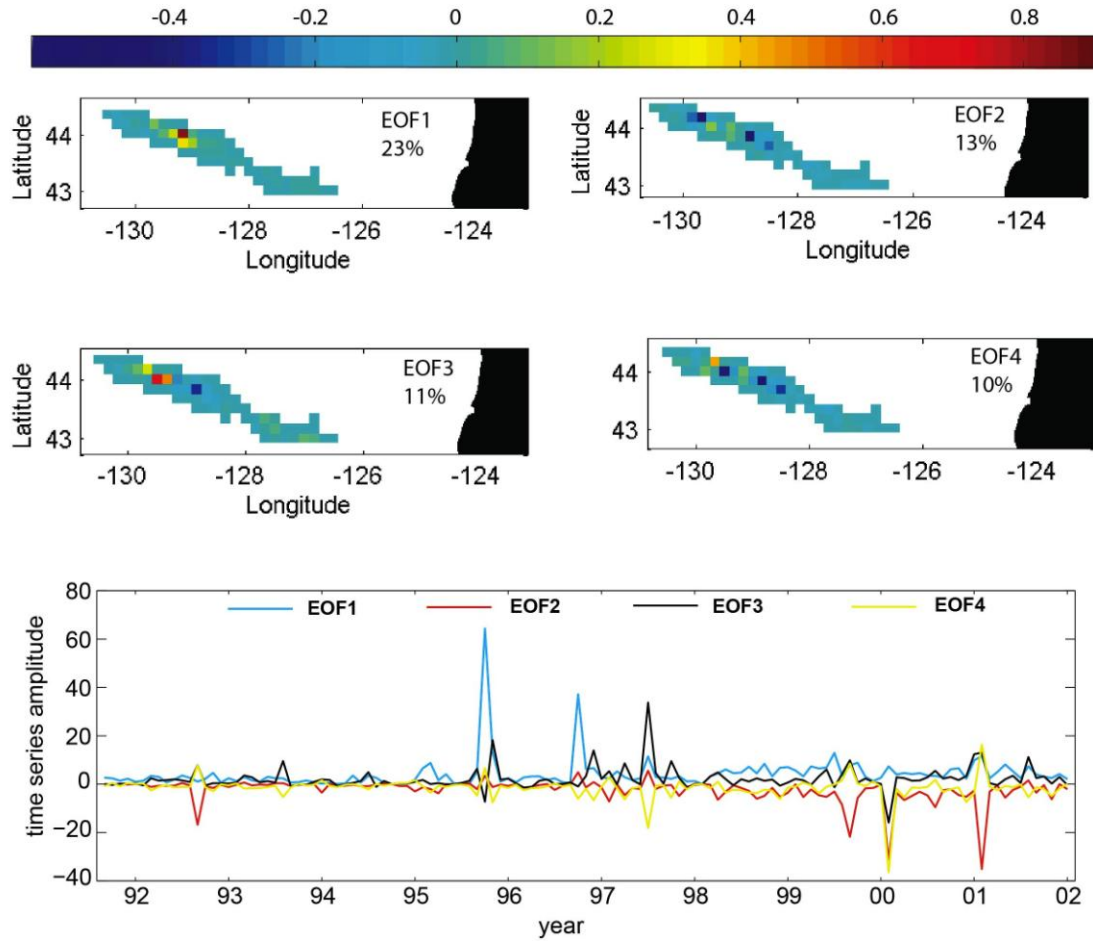


Figure 2.12 Blanco transform EOF modes, eigenvalues (% variance), and time series amplitudes.

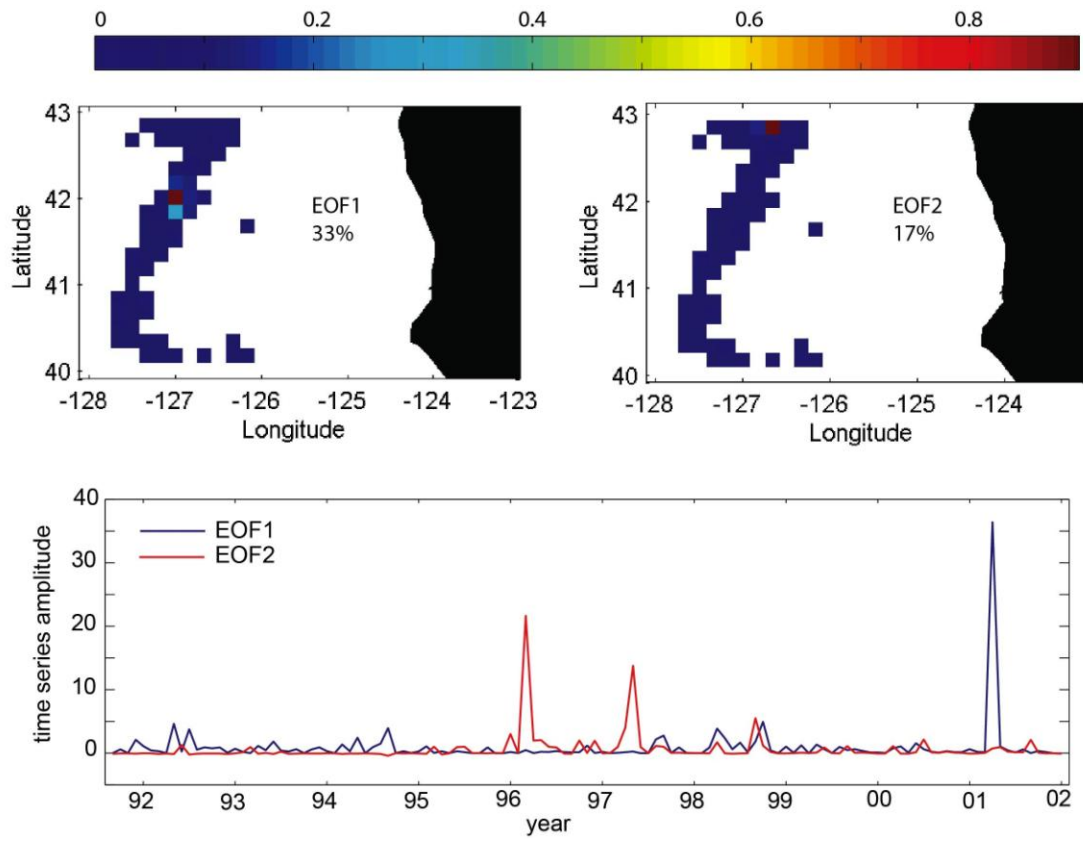


Figure 2.13 Gorda ridge EOF modes, eigenvalues (% variance), and time series amplitudes.

2.8 REFERENCES

- Bohnenstiehl, D. R., Dziak, R. P., Tolstoy, M., Fox, C. G., and Fowler, M., 2004a, Temporal and spatial history of the 1999–2000 Endeavour Segment seismic series, Juan de Fuca Ridge: *Geochem. Geophys. Geosyst.*, v. 5.
- , 2004b, Temporal and spatial history of the 1999–2000 Endeavour Segment seismic series, Juan de Fuca Ridge: *Geochem. Geophys. Geosyst.*, v. 5.
- Bohnenstiehl, D. R., Tolstoy, M., Dziak, R. P., Fox, C. G., and Smith, D. K., 2002, Aftershock sequences in the mid-ocean ridge environment: an analysis using hydroacoustic data: *Tectonophysics*, v. 354, no. 1-2, p. 49-70.
- Braunmiller, J., and Nábělek, J., 2008, Segmentation of the Blanco Transform Fault Zone from earthquake analysis: Complex tectonics of an oceanic transform fault: *Journal of Geophysical Research: Solid Earth (1978–2012)*, v. 113, no. B7.
- Cronin, V. S., and Sverdrup, K. A., 2003, Multiple-event relocation of historic earthquakes along Blanco Transform Fault Zone, NE Pacific: *Geophysical Research Letters*, v. 30, no. 19, p. 2001.
- Davis, E., Becker, K., Dziak, R., Cassidy, J., Wang, K., and Lilley, M., 2004, Hydrological response to a seafloor spreading episode on the Juan de Fuca ridge: *Nature*, v. 430, no. 6997, p. 335-338.
- Dziak, R. P., 2001, Empirical relationship of T-wave energy and fault parameters of northeast Pacific Ocean earthquakes: *Geophysical Research Letters*, v. 28, no. 13, p. 2537-2540.
- , 2006, Explorer deformation zone: Evidence of a large shear zone and reorganization of the Pacific–Juan de Fuca–North American triple junction: *Geology*, v. 34, no. 3, p. 213-216.
- Dziak, R. P., Chadwick, W. W., Fox, C. G., and Embley, R. W., 2003, Hydrothermal temperature changes at the southern Juan de Fuca Ridge associated with Mw 6.2 Blanco Transform earthquake: *Geology*, v. 31, no. 2, p. 119-122.
- Dziak, R. P., and Fox, C. G., 1999, The January 1998 earthquake swarm at Axial Volcano, Juan de Fuca Ridge: Hydroacoustic evidence of seafloor volcanic activity: *Geophysical Research Letters*, v. 26, no. 23, p. 3429-3432.
- Dziak, R. P., Fox, C. G., and Schreiner, A. E., 1995, The June–July 1993 seismo-acoustic event at CoAxial segment, Juan de Fuca Ridge: Evidence for a lateral dike injection: *Geophysical Research Letters*, v. 22, no. 2, p. 135-138.

- Dziak, R. P., Fox, C. G., and Slack, P. D., 1996, T wave source level and earthquake fault parameters: Empirically derived scaling relationships: *The Journal of the Acoustical Society of America*, v. 100, p. 2639.
- Dziak, R. P., Hammond, S. R., and Fox, C. G., 2011, A 20-year hydroacoustic time series of seismic and volcanic events in the Northeast Pacific Ocean: *Oceanography*-Oceanography Society, v. 24, no. 3, p. 280.
- Fox, C. G., Cowen, J. P., Dziak, R. P., Baker, E. T., Embley, R. W., Chadwick, W. W., Lupton, J. E., Resing, J. A., and Hammond, S. R., Detection and response to a seafloor spreading episode on the central Gorda Ridge, April 2001, in *Proceedings American Geophysical Union 2001 Fall Meeting*, San Francisco, CA, 2001a, Volume 1, p. 05.
- Fox, C. G., and Dziak, R. P., 1998, Hydroacoustic detection of volcanic activity on the Gorda Ridge, February–March 1996: *Deep Sea Research Part II: Topical Studies in Oceanography*, v. 45, no. 12, p. 2513-2530.
- , 1999, Internal deformation of the Gorda Plate observed by hydroacoustic monitoring: *Journal of Geophysical Research: Solid Earth* (1978–2012), v. 104, no. B8, p. 17603-17615.
- Fox, C. G., Matsumoto, H., and Lau, T. K. A., 2001b, Monitoring Pacific Ocean seismicity from an autonomous hydrophone array: *Journal of Geophysical Research*, v. 106, no. B3, p. 4183-4206.
- Fox, C. G., Radford, W. E., Dziak, R. P., Lau, T. K., Matsumoto, H., and Schreiner, A. E., 1995, Acoustic detection of a seafloor spreading episode on the Juan de Fuca Ridge using military hydrophone arrays: *Geophysical Research Letters*, v. 22, no. 2, p. 131-134.
- Frohlich, C., and Davis, S. D., 1990, Single Link Cluster Analysis As A Method to Evaluate Spatial and Temporal Properties of Earthquake Catalogues: *Geophysical Journal International*, v. 100, no. 1, p. 19-32.
- Goltz, C., 2001, Decomposing spatio-temporal seismicity patterns: *Natural Hazards and Earth System Science*, v. 1, no. 1/2, p. 83-92.
- Holliday, J. R., Chen, C.-c., Tiampo, K. F., Rundle, J. B., Turcotte, D. L., and Donnellan, A., 2007, A RELM earthquake forecast based on pattern informatics: *Seismological Research Letters*, v. 78, no. 1, p. 87-93.
- Preisendorfer, R. W., and Mobley, C. D., 1988, *Principal component analysis in meteorology and oceanography*, 425 pp, Elsevier Sci., New York.

- Rundle, J. B., Klein, W., Tiampo, K., and Gross, S., 2000, Linear pattern dynamics in nonlinear threshold systems: *Physical Review E*, v. 61, no. 3, p. 2418.
- Teague, W. J., Carron, M. J., and Hogan, P. J., 1990, A comparison between the Generalized Digital Environmental Model and Levitus climatologies: *Journal of Geophysical Research: Oceans* (1978–2012), v. 95, no. C5, p. 7167-7183.
- Tiampo, K. F., Rundle, J. B., McGinnis, S. A., and Klein, W., 2002, Pattern dynamics and forecast methods in seismically active regions: *Pure and Applied Geophysics*, v. 159, p. 2429-2467.
- Tolstoy, I., and Ewing, M., 1950, The T phase of shallow-focus earthquakes: *Bulletin of the Seismological Society of America*, v. 40, no. 1, p. 25.

**3 SEISMIC CYCLES, SEAFLOOR DEFORMATION AND VOLCANIC
ERUPTIONS AT AXIAL SEAMOUNT, JUAN DE FUCA RIDGE**

Joseph H. Haxel, Robert P. Dziak, T.K. Lau, William W. Chadwick and Scott L.
Nooner

To be submitted to *Geology*

3.1 ABSTRACT

Over the past 20 years, continuous seismic monitoring efforts have recorded earthquakes preceding two remarkably similar deep-ocean volcanic eruptions at Axial Seamount on the Juan de Fuca Ridge. A network of U.S. Navy hydrophone arrays (SOSUS) detecting regional seismic activity from 1991- present captured the increase in seismic activity leading to a magmatic intrusion and eruption in January 1998 and a small array of ocean bottom hydrophones (OBHs) deployed in and around the caldera (Sep. 7, 2006 - present) provide a multi-year record of local micro-seismicity (< 2.5 Mb) at Axial preceding the subsequent seafloor eruption in April 2011. A total of 16,329 earthquakes in and around Axial Seamount were identified on the local OBH network from September 2006 – July 2011. Earthquake hypocenters preceding the 2011 volcanic event are focused near the SE corner of the caldera at depths generally ranging from 1.5-2 km below the seafloor. Earthquake rate counts compared with seafloor deformation measurements show a rise in background seismicity levels over several months, coincident with an increase in the rate of uplift at the center of the caldera. On smaller time scales, individual seismic swarms are uncorrelated with short-term variability in the seafloor geodetic measurements.

3.2 INTRODUCTION

Monitoring seismic activity and ground deformation are two of the most effective methods for tracking subsurface magmatic migration within volcanic systems. Intrusions at seafloor volcanic rift zones often produce intense periods of seismic energy release triggered by elevated crustal stresses accompanying ascending and laterally propagating dikes. Characterizing the temporal and spatial patterns of

increasing seismic activity in the years and months prior to eruptions provides valuable information to aid in the forecasting of future events. Similarly, long-term seafloor deformation measurements afford independent and complementary information, linking subsurface magma supply with varying levels of seismic activity. The remote nature and extreme conditions of deep sea environments has limited continuous seismic recordings and ground deformation measurements at seafloor spreading centers, resulting in few direct observations of a complete seismic cycle between eruptive events. Here, we use acoustic records from regional and local hydrophone arrays, spanning 20 years and two seafloor eruptions, to document earthquake activity from Axial Seamount on the Juan de Fuca Ridge. This study investigates the long-term patterns in seismic activity levels in relation to ground deformation measurements leading toward submarine volcanic eruptions.

3.3 BACKGROUND

Axial Seamount is an active submarine volcano located at the intersection of the Juan de Fuca Ridge with the southern terminus of the Cobb-Eickelberg Seamount chain, where hot-spot mantle upwelling converges with mid-ocean ridge rifting ~450 kilometers west of the Oregon coast in the northeast Pacific Ocean (Fig. 3.1). The two most recent intrusions/eruptions at Axial occurred in 1998 (Chadwick et al., 2013; Embley et al., 1999) and 2011 (Caress et al., 2012; Chadwick Jr et al., 2012) separated by 13 years. Each event was accompanied by thousands of earthquakes; the first recorded by regional hydrophone networks in January 1998 (Dziak and Fox, 1999b), and the latest observed with in-situ instrumentation in April 2011 (Dziak et al., 2012). Restricted access to the U.S. Navy SOSUS regional hydrophone arrays

since 1991 allowed for continuous seismic monitoring of Axial Seamount, including the gradual increase in seismic energy ($M_b > 2.5$) during the seven years prior to the eruption in 1998 (Dziak and Fox, 1999a) as well as the quiescent post eruptive period in the following years.

In addition to the long-term regional seismic record from SOSUS, two localized microearthquake studies before and after the 1998 eruption provide “snapshot” views of pre and post intrusion seismicity rates. A three element array of ocean bottom seismometers (OBS), deployed for two months during the summer of 1994, located 402 micro-earthquakes ($M_b < 2.5$) focused mostly near the southeastern area of the caldera (Tolstoy et al., 2002). Additionally, two weeks after the 1998 eruption, a local OBS array was deployed, providing a record of low-level, microseismicity ($M_b < 2.5$) associated with cooling and contraction of the intruded magmas (Sohn et al., 2004; Sohn et al., 1999). In 2003, the detection sensitivity of the SOSUS hydrophone network for volcanic activity at Axial Seamount began to degrade with the loss of some key elements within the arrays. This prompted the long-term deployment and maintenance of an ocean bottom hydrophone (OBH) array for local seismic monitoring from September 2006 to the present. SOSUS cable breaks in December 2009 resulted in greatly diminished seismic detection capability in the NE Pacific (including during the 2011 eruption) further emphasizing the importance of the local OBH array at Axial.

3.4 METHODS

3.4.1 Instrumentation and Data

OBH platforms were deployed on the seafloor in and around the southern portion of Axial caldera (Fig. 3.1) to capture magmatically driven seismic activity in a known area of microearthquake clustering (Sohn et al., 2004; Tolstoy et al., 2002) that overlies a mid-crustal melt reservoir (West et al., 2001). The OBH instruments have sensitivity $-192 \mu\text{Pa V}^{-1}$ and record at a sample rate of 250 Hz with an anti-aliasing filter cutoff of 110 Hz, providing continuous pressure measurements in the 0.1 – 110 Hz frequency band. OBH's were recovered and redeployed at yearly intervals documenting nearly five years of microearthquake activity leading to the eruption in April 2011.

Microearthquake data processing in this study utilizes an automated detection algorithm (Mellinger, 2001) tuned for low frequency hydroacoustic earthquake energy that is applied to the raw hydrophone data. Detection of an earthquake arrival is triggered when the summation of spectral energy in the $0.1 \text{ Hz} < f < 10 \text{ Hz}$ band calculated from a 1-second data block exceeds the energy summed over an 8 second window by a factor of 2. Seismic arrivals detected on at least 3 hydrophones within a 10 second window are associated with an earthquake event. Events are then filtered by visual inspection to a subset of seismicity based on P and PwP phase arrivals unique to local microearthquakes at Axial Seamount ((Sohn et al., 2004); Fig. 3.2), excluding the emergent seismic arrivals associated with more distant events. Using this approach 16,329 microearthquakes in and around Axial Seamount were identified on the local OBH networks from September 2006 – July 2011.

3.4.2 Hypocentral Estimates

Typical array deployments consisted of up to three OBHs. In 2009-2010, four OBH stations were deployed allowing for hypocentral estimates using hand-picked P phase seismic arrivals. Unfortunately, an instrument gain problem with the southern hydrophone severely limited the identification of P and P_wP phases that were recorded on the other 3 OBH's. A grid search algorithm based on velocities from a seismic refraction experiment (West et al., 2001) around Axial Seamount was used to obtain hypocenters for a small subset of earthquakes located within the array where P phase arrivals could be identified on all four OBH's (Fig. 3.1). Model P phase travel time grids ($dx = 1$ km; $dy = 1$ km; $dz = 0.25$ km) were calculated for each station using the harmonic mean of the velocities encountered along the ray path from a grid cell to each station. Earthquake hypocentral locations were identified by the grid cell with the minimum root mean squared residual from the difference between modeled and observed P phase travel times. Confidence intervals were estimated by applying the Student's t -statistic (1 degree of freedom, 95% probability) to the root mean squared residuals (in seconds), and multiplying by the x,y,z directional harmonic mean velocity components from the modeled travel time grids to obtain standard error estimates in kilometers. Applying this grid search method approach produced hypocentral estimates for 42 microearthquakes located within one aperture of the four station OBH array during the 2009-2010 deployment.

3.5 RESULTS AND DISCUSSION

3.5.1 Seismic Cycles

In the years immediately following the dike intrusion and eruptive events at Axial, seismic activity levels remained low (Dziak and Fox, 1999a; Sohn et al., 1999) and are linked with thermal processes and cooling around the caldera (Sohn et al., 2004). Utilizing earthquake counts as a measure of seismic activity level, both regional SOSUS and local OBH data exhibit steady increases in seismicity during the 2-3 years preceding the 1998 and 2011 intrusion and seafloor eruptive events (Fig. 3.3). Despite the difference in detection threshold between the regional and local hydrophone arrays, the observed earthquake counts reveal similar patterns showing an increase in earthquake swarm occurrence as well as growing numbers of earthquakes per swarm. Swarms consisting of > 50 microearthquakes are observed on the OBH array beginning April 2009, occurring with increasing frequency during the two years leading up to the April 2011 eruption (Fig. 3.3b). This pattern is similar to the increasing size and frequency of larger seismic swarms (≥ 50 events) detected by the regional SOSUS hydrophone array beginning in May 1996 building toward the January 1998 eruption at Axial (Dziak and Fox, 1999a). These elevated background seismicity levels suggest building of crustal stresses from rising magma pressures induce increasingly frequent seismic failure ~ 2 years prior to the larger dike intrusion events at Axial. Future forecasting of magmatic events may be aided by the basic earthquake rate counts used here, and by employing a threshold measure of the total seismic moment release afforded by the ocean bottom seismometer instrumentation

planned for deployment in association with the Ocean Observatories Initiative (OOI, 2013).

Analogous, subaerial rift-zone/ hot-spot volcanic systems in Iceland (Einarsson and Brandsdottir, 1980; Pedersen et al., 2007; Sturkell et al., 2003; Tryggvason, 1994) and the Afar region of NE Africa (Wright et al., 2012) have shown similar increases in background seismic activity levels preceding major dike intrusions, but over longer time periods. Whereas the volcanic cycle of these on-land systems exhibit rifting episodes and eruptive activity lasting up to a decade separated by quiet periods on the order of centuries, Axial appears to experience volcanic unrest on a decadal time scale punctuated by single intrusions. The observed dissimilarities in volcanic cycles are likely linked to differences in plate divergence rates, magma supply, and crustal thicknesses from the faster/thinner intermediate Juan de Fuca Ridge to the slower/thicker spreading regimes of the Mid-Atlantic Ridge and Afar Rift.

3.5.2 Microearthquake Locations

Epicentral locations from the 2009-2010 OBH deployment are focused in the southeast region of the caldera and rim wall (Fig. 3.1), consistent with results from previous microearthquake studies at Axial (Sohn et al., 2004; Sohn et al., 1999; Tolstoy et al., 2002). Origin times of the 42 microearthquakes span the deployment period, but are largely concentrated within the first three months (June-August 2009). The clustered location of these microearthquakes near and around the 2011 eruptive vents (Caress et al., 2012) suggests that episodic variations in magma pressure within an underlying melt body, may have been causing brittle failure and seismic energy

release in the overlying crustal rock, years prior to the intrusion event. Hypocentral depth estimates projected onto a cross sectional profile across the caldera (Fig. 3.1) are plotted over the P wave velocity model (West et al., 2001) in Figure 3.4, showing the majority of microseismicity associated with this subset of earthquakes occurs in the upper 1.5 km of crust above a low velocity melt zone. Depth estimates below this magma body are not well constrained, exhibiting a larger amount of uncertainty likely associated with timing error in P wave arrivals. Data from the OBH array is limited to hypocentral locations, lacking focal mechanism and seismic moment release information that would enable further geophysical interpretation of these events.

3.5.3 Microearthquakes and Seafloor Deformation

Long-term seafloor deformation measurements at Axial Seamount show rapid re-inflation of the central caldera floor that steadily decays to a linear rate in the first few years following an eruptive event (Chadwick et al., 2012; Chadwick et al., 2006; Nooner and Chadwick, 2009). Despite the high post-eruptive uplift rate, this period of rapid re-inflation occurs aseismically, with background earthquake activity levels dropping significantly below pre-intrusion rates (Fig. 3.5a), probably because the pressure in the subcaldera magma reservoir is at a minimum. A conceptual model of initial recharge based on viscoelastic relaxation and porous flow of melt from the partial melt zone beneath the magma chamber is consistent with the lack of observed seismicity (Nooner and Chadwick, 2009).

After the initial rapid re-inflation, a lower longer-term steady influx of magma from a deep source provides a linear rate of seafloor uplift (Nooner and Chadwick,

2009). A gradual increase in the inflation rate at the center of the caldera in the months before an eruption (Chadwick et al., 2012) is mimicked by a gradual increase in the background seismicity levels. However, on the shorter time scales of individual earthquake swarms, seismic activity and seafloor uplift remain uncorrelated (Fig. 3.5). This is in contrast to the connection observed between seafloor deformation and seismic swarms observed prior to the 1998 eruption (Dziak and Fox, 1999a). The modeled constant rate of influx to the magma chamber from a deep source provides a steady rate of seafloor uplift measured in the central caldera unrelated to the episodic bursts in seismic activity, suggesting the seismic response of the overlying crust to rising magma pressures is a complex combination of stress relief and slip that takes place at depth immediately surrounding the subcaldera magma reservoir, and is not always measured at the ground surface.

3.6 SUMMARY

Long-term hydroacoustically derived seismic records of Axial Seamount show patterns of increasing frequency and intensity for large (> 50) earthquake swarms roughly 2 years prior to the magmatic intrusion events observed in 1998 and 2011. Hypocentral estimates from the most well constrained, locally recorded events indicate seismicity clusters in the upper 1.5-2 km of crust in the SE corner of the caldera during the years preceding volcanic eruptions on the upper south rift zone. Long-term deformation and seismicity signals are similar on time scales of months to years, but do not correlate on the time scale of individual earthquake swarms (hours

to days), suggesting the influence of a steady influx of magma from a deep seated source may not be reflected by higher frequency variability in earthquake rate counts.

Instead of decade long periods of seismic and volcanic unrest separated by centuries that has been observed at land based rift zone/ hotspot volcanic centers, Axial Seamount displays decadal scale cycles punctuated by single eruptive events. The difference in the seismic and volcanic cycles between the regimes suggests the Axial volcanic system may behave more regularly, allowing for improved forecasting of future seafloor eruptions.

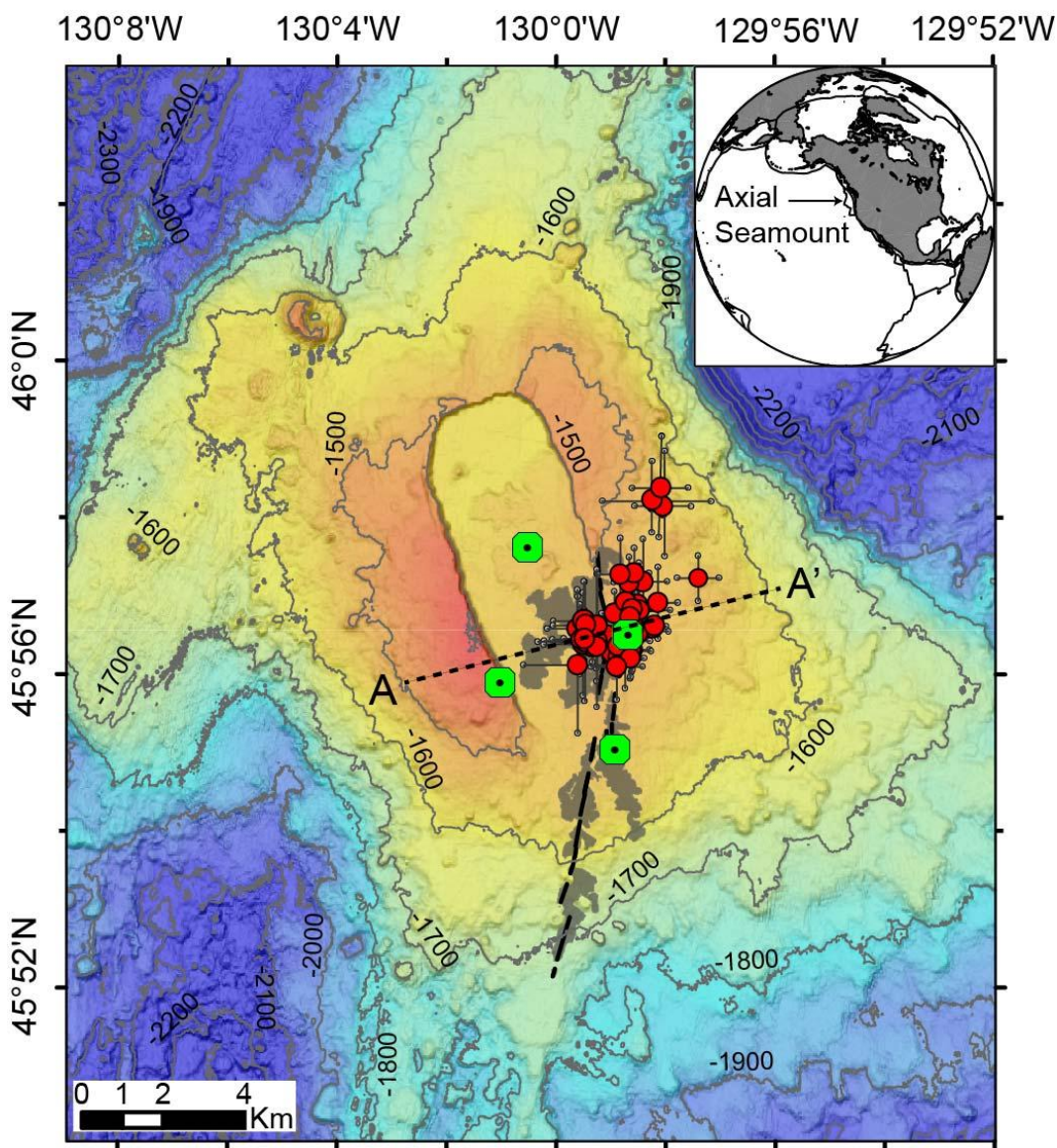


Figure 3.1 Map of Axial Seamount showing the locations of the ocean bottom hydrophones (OBHs; green circles), the epicentral locations and associated error of a small subset of earthquakes from 2009-2010 (red circles), the lava flows (gray) and eruptive vents (black lines) from the 2011 eruption (Caress et al., 2012), and the profile across the caldera (A-A') used for depth projections in Figure 3.4. Depth contours are shown in meters below the sea surface.

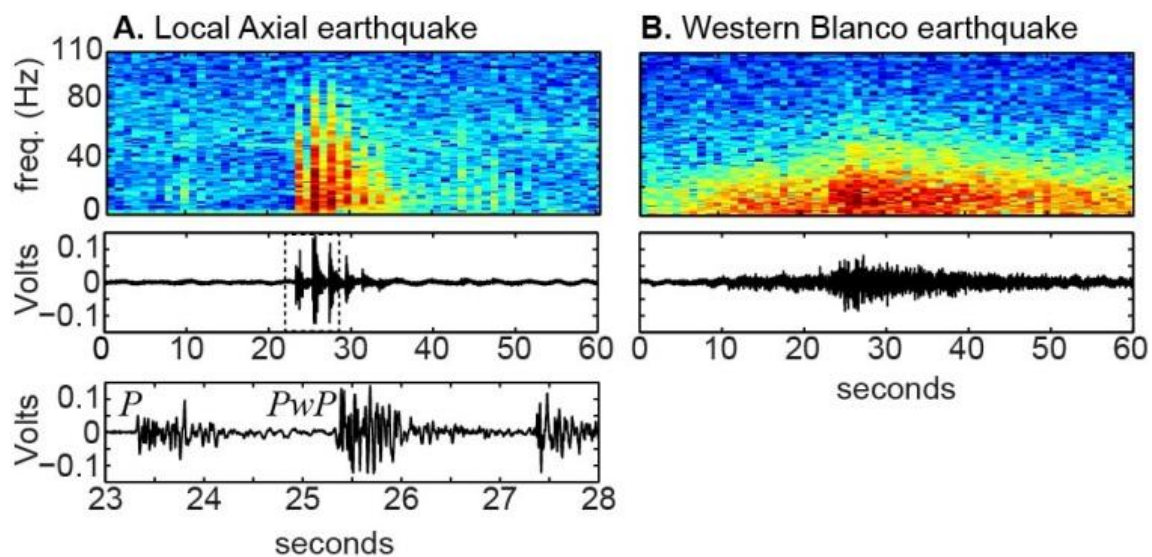


Figure 3.2 Frequency and waveform displays of seismic energy recorded on the OBH array by A) a locally generated earthquake and B) an earthquake from the Western Blanco Transform Fault. The bottom panel from (A) shows a zoomed in view of the P arrival and subsequent reflected PwP phase used to identify local earthquakes.

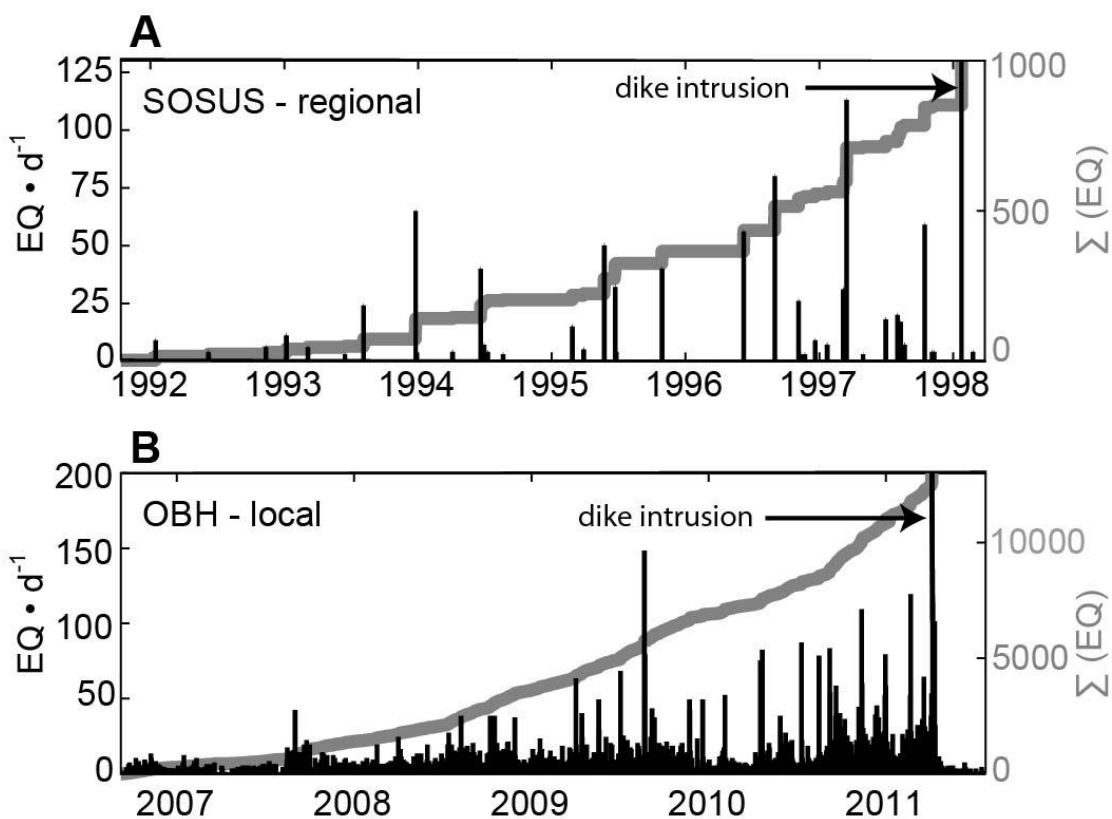


Figure 3.3. A) The number of earthquakes detected in each swarm by the SOSUS hydrophone arrays prior to the 1998 seafloor eruption (after Dziak and Fox, 1999a). B) Earthquake counts recorded by the in-situ OBH array preceding the 2011 volcanic eruption. Cumulative events are shown as continuous thick gray lines.

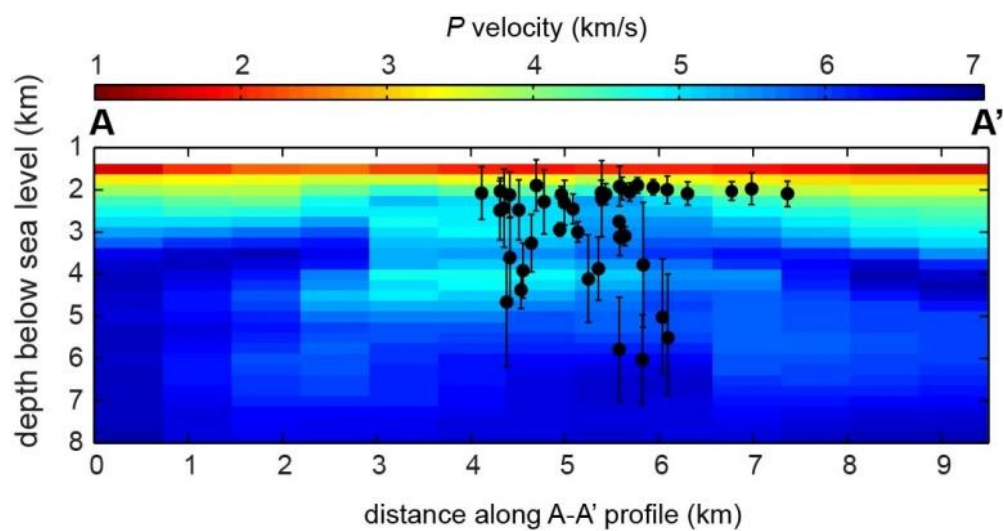


Figure 3.4. Hypocentral locations and error estimates projected onto a profile across the caldera (A-A') from Figure 3.1, overlain on the P wave velocity model from West et al. (2001).

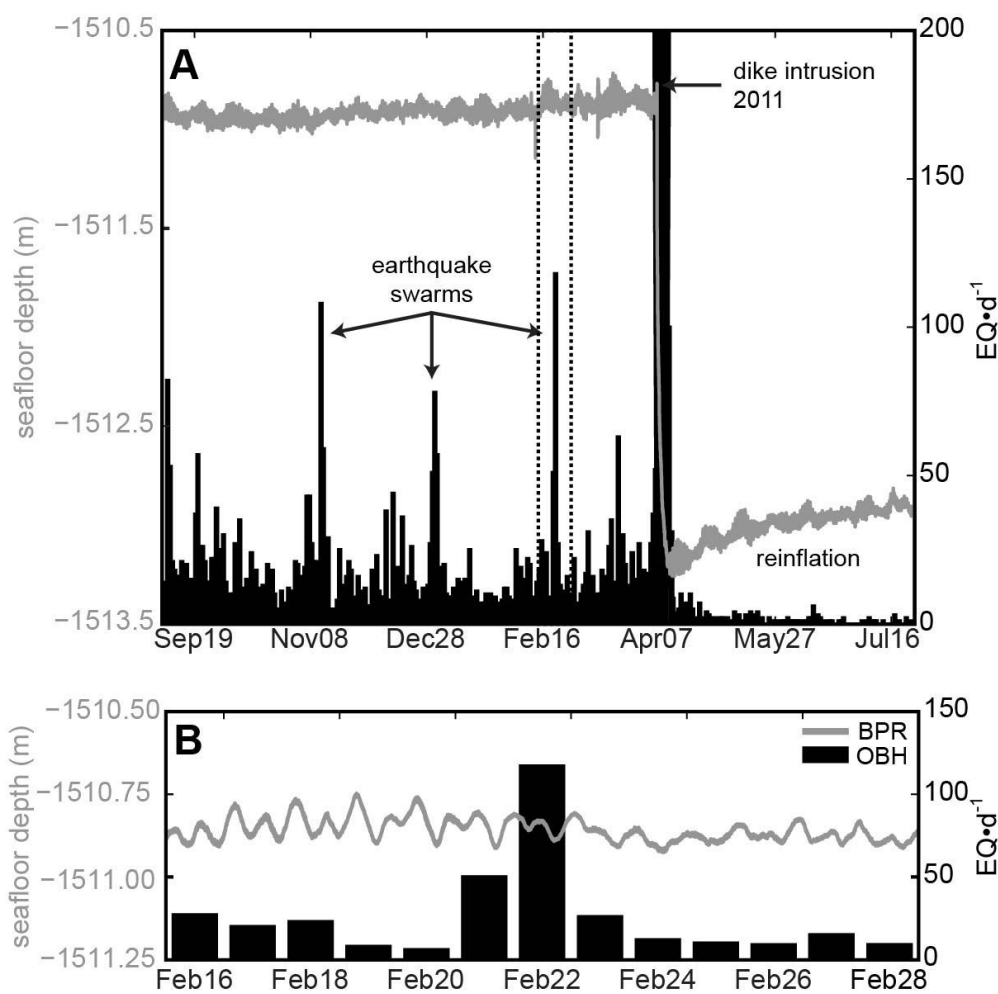


Figure 3.5 A) Nearly year-long record from a bottom pressure recorder on the seafloor in the central caldera showing the preceding slow uplift and abrupt co-eruptive deflation at the time of maximum seismic energy release in 2011. B) A zoomed view from the dashed box in (A) of the earthquake rate and geodetic measurement time series showing the absence of significant seafloor deformation accompanying a large seismic swarm in the months prior to the 2011 intrusion/eruption.

3.7 REFERENCES

- Caress, D. W., Clague, D. A., Paduan, J. B., Martin, J. F., Dreyer, B. M., Chadwick Jr, W. W., Denny, A., and Kelley, D. S., 2012, Repeat bathymetric surveys at 1-metre resolution of lava flows erupted at Axial Seamount in April 2011: *Nature Geoscience*, v. 5, no. 7, p. 483-488.
- Chadwick, W. W., Nooner, S. L., Butterfield, D. A., and Lilley, M. D., 2012, Seafloor deformation and forecasts of the April 2011 eruption at Axial Seamount: *Nature Geoscience*, v. 5, no. 7, p. 474-477.
- Chadwick, W. W., Clague, D. A., Embley, R. W., Perfit, M. R., Butterfield, D. A., Caress, D. W., Paduan, J. B., Martin, J. F., Sasnett, P., and Merle, S. G., 2013, The 1998 eruption of Axial Seamount: New insights on submarine lava flow emplacement from high- resolution mapping: *Geochemistry, Geophysics, Geosystems*, in press.
- Chadwick, W. W., Nooner, S. L., Zumberge, M. A., Embley, R. W., and Fox, C. G., 2006, Vertical deformation monitoring at Axial Seamount since its 1998 eruption using deep-sea pressure sensors: *Journal of Volcanology and Geothermal Research*, v. 150, no. 1-3, p. 313-327.
- Dziak, R. P., and Fox, C. G., 1999a, Long-term seismicity and ground deformation at Axial Volcano, Juan de Fuca Ridge: *Geophysical Research Letters*, v. 26, no. 24, p. 3641-3644.
- , 1999b, The January 1998 earthquake swarm at Axial Volcano, Juan de Fuca Ridge: Hydroacoustic evidence of seafloor volcanic activity: *Geophysical research letters*, v. 26, no. 23, p. 3429-3432.
- Dziak, R. P., Haxel, J. H., Bohnenstiehl, D. R., Chadwick, W. W., Nooner, S. L., Fowler, M. J., Matsumoto, H., and Butterfield, D. A., 2012, Seismic precursors and magma ascent before the April 2011 eruption at Axial Seamount: *Nature Geoscience*, v. 5, no. 7, p. 478-482.
- Einarsson, P., and Brandsdottir, B., 1980, Seismological evidence for lateral magma intrusion during the July 1978 deflation of the Krafla volcano in NE Iceland: *Journal of Geophysics-Zeitschrift Fur Geophysik*, v. 47, no. 1-3, p. 160-165.
- Embley, R. W., Chadwick Jr, W. W., Clague, D., and Stakes, D., 1999, 1998 eruption of axial volcano: Multibeam anomalies and sea-floor observations: *Geophysical Research Letters*, v. 26, no. 23, p. 3425-3428.
- Mellinger, D. K., 2001, Ishmael 1.0 user's guide: NOAA Technical Memorandum OAR PMEL, v. 120, no. 26, p. 98115-96349.

- Nooner, S. L., and Chadwick, W. W., 2009, Volcanic inflation measured in the caldera of Axial Seamount: Implications for magma supply and future eruptions: *Geochemistry Geophysics Geosystems*, v. 10.
- Ocean Observatories Initiative (OOI), 2013, <http://www.ooi/washington.edu/>.
- Pedersen, R., Sigmundsson, F., and Einarsson, P., 2007, Controlling factors on earthquake swarms associated with magmatic intrusions; Constraints from Iceland: *Journal of Volcanology and Geothermal Research*, v. 162, no. 1-2, p. 73-80.
- Sohn, R. A., Barclay, A. H., and Webb, S. C., 2004, Microearthquake patterns following the 1998 eruption of Axial Volcano, Juan de Fuca Ridge: Mechanical relaxation and thermal strain: *Journal of Geophysical Research-Solid Earth*, v. 109, no. B1, p. 14.
- Sohn, R. A., Crawford, W. C., and Webb, S. C., 1999, Local seismicity following the 1998 eruption of Axial Volcano: *Geophysical Research Letters*, v. 26, no. 23, p. 3433-3436.
- Sturkell, E., Sigmundsson, F., and Einarsson, P., 2003, Recent unrest and magma movements at Eyjafjallajökull and Katla volcanoes, Iceland: *Journal of Geophysical Research*, v. 108, no. B8, p. 2369.
- Tolstoy, M., Vernon, F. L., Orcutt, J. A., and Wyatt, F. K., 2002, Breathing of the seafloor: Tidal correlations of seismicity at Axial volcano: *Geology*, v. 30, no. 6, p. 503-506.
- Tryggvason, E., 1994, Surface deformation at the Krafla volcano, North Iceland, 1982-1992: *Bulletin of Volcanology*, v. 56, no. 2, p. 98-107.
- West, M., Menke, W., Tolstoy, M., Webb, S., and Sohn, R., 2001, Magma storage beneath Axial volcano on the Juan de Fuca mid-ocean ridge: *Nature*, v. 413, no. 6858, p. 833-836.
- Wright, T. J., Sigmundsson, F., Pagli, C., Belachew, M., Hamling, I. J., Brandsdóttir, B., Keir, D., Pedersen, R., Ayele, A., and Ebinger, C., 2012, Geophysical constraints on the dynamics of spreading centres from rifting episodes on land: *Nature Geoscience*, v. 5, no. 4, p. 242-250.

**4 OBSERVATIONS OF SHALLOW WATER MARINE AMBIENT SOUND:
THE LOW FREQUENCY UNDERWATER SOUNDSCAPE OF THE
CENTRAL OREGON COAST**

Joseph H. Haxel, Robert P. Dziak and Haru Matsumoto

Published in *The Journal of the Acoustical Society of America*
2 Huntington Quadrangle
Suite 1NO1
Melville, NY 11747-4502
2013, Vol. 133, Issue 5, pp. 2586-2596 (11 pages)

4.1 ABSTRACT

A year-long experiment (March 2010 to April 2011) measuring ambient sound at a shallow water site (50 m) on the central Oregon coast near the Port of Newport provides important baseline information for comparisons with future measurements associated with resource development along the inner continental shelf of the Pacific Northwest. Ambient levels in frequencies affected by surf-generated noise ($f < 100$ Hz) characterize the site as a high-energy end member within the spectrum of shallow water coastal areas influenced by breaking waves. Dominant sound sources include locally generated ship noise (66% of total hours contain local ship noise), breaking surf, wind induced wave breaking and baleen whale vocalizations. Additionally, an increase in spectral levels for frequencies ranging from 35-100 Hz is attributed to noise radiated from distant commercial ship commerce. One-second root mean square sound pressure level (SPL_{rms}) estimates calculated across the 10-840 Hz frequency band for the entire year long deployment show minimum, mean, and maximum values of 84 dB, 101 dB, and 152 dB *re* 1 μ Pa.

4.2 INTRODUCTION

Multi-year, decadal trends in coastal shallow water ambient noise levels are difficult to measure resulting mostly from the rarity of repeated long-term acoustic recordings. Localized propagation effects, environmental conditions and inconsistent anthropogenic sound sources make comparisons between shallow water sites speculative. Nevertheless, data sets similar to the one presented here are essential for not only providing baseline information in assessing future measurements of ambient

noise levels on local and possibly regional scales, but also for identifying where a site fits within the range of noise levels observed in a variety of shallow water coastal environments. Characterizations of the frequency structure and time dependency of natural and anthropogenic sound sources included in this study provide context for a description of time-averaged spectral level measurements at this site and similar coastal areas along the inner continental shelf of the Pacific Northwest. Similarly, the distribution of sound pressure level estimates indicates how commonly a particular acoustic energy level is reached, providing valuable information for regulatory agencies on background levels.

Ambient sound levels are a critical component for the environmental health of ocean ecosystems (NRC, 2005). Marine mammals have evolved to use sound for communication, navigation, and stalking prey (Au, 1993; Edds-Walton, 1997), taking advantage of the efficient propagation of acoustic energy in the oceans. Similarly, fish navigate, communicate, mate, and choose habitat based on acoustic criteria (Simpson *et al.*, 2005). Characterizing baseline natural and anthropogenic contributions to ambient noise levels is therefore critical for assessing the impacts of future man-made increases in sound levels on marine habitat (Hildebrand, 2009). The potential effects of long-term exposure to increasing ambient noise on marine organisms are not well understood, and may not be easily recognized from short-term observation of behavioral changes. Instead, extended effects may potentially manifest as subtle long-term variations in behavior (Picciulin *et al.*, 2010), chronic stress (Wright *et al.*, 2007), and masking of important biological signals (Clark *et al.*, 2009).

Long-term deep ocean acoustic measurements of rising ambient noise in the northeast Pacific since the 1960s are well documented and associated primarily with increases in commercial shipping (Andrew *et al.*, 2002; McDonald *et al.*, 2006; Chapman and Price, 2011). Meanwhile, comparisons of shallow water ambient sound at a single site over several decades are limited (Wenz, 1964; McDonald *et al.*, 2008) and lack a similar long-term increase in noise levels. Comparisons of long-term ambient levels between shallow water sites are problematic at frequencies below ~ 500 Hz (Wenz, 1962). The acoustic propagation effects related to complex local bathymetry and seafloor properties, variations in sound energy radiated by vessel traffic, and physical processes particular to the environmental conditions at each shallow coastal site contribute to invalid time dependent comparisons of trending noise levels.

4.3 BACKGROUND

Ambient noise level measurements in the continental shelf waters off the Pacific Northwest coast of North America have received little attention. The high-energy conditions and perennial fishing activity present unique challenges to long-term mooring survival. Despite these challenges, further resource development and human activities within the territorial seas are imminent, prompting an urgent need for baseline information on ambient noise levels in these shallow coastal zones. The Northwest National Marine Renewable Energy Center (NNMREC) in affiliation with Oregon State University has established an ocean test facility (OTF) in state waters off the coast of Oregon (Fig. 4.1, <http://nnmrec.oregonstate.edu/node/85>). The

purpose of the OTF is to provide an accredited, standardized resource for wave energy conversion developers to perform ocean testing of their devices.

The region surrounding the OTF provides important habitat for fish, benthic fauna and a number of actively vocal transitory and local Mysticeti species, including humpback, fin, blue, and gray whales. In particular, roughly 19,000 eastern North Pacific gray whales (*Eschrichtius robustus*) migrate through these waters from their northern feeding grounds in the Chukchi and Bering seas to the calm waters of Baja California during calving season and then back again (Herzing and Mate, 1984). Ambient noise levels aid in their passive navigation as this species of whale moves along its migratory route (Wladichuk *et al.*, 2008). The acoustic impacts on marine habitat resulting from the installation and operation of the OTF should be minimized and can only be assessed from comparative studies using baseline ambient noise measurements. Recordings from a 1/7th scale wave energy conversion buoy in Puget Sound indicate the largest acoustic contribution to ambient levels from this type of device occurs in frequencies below 1 kHz (Bassett *et al.*, 2011). This study provides an initial baseline description of long-term ambient noise levels and sound sources in the 10-840 Hz frequency range that can be utilized for future comparisons with ocean testing of wave energy conversion devices at NNMREC's OTF near Newport, Oregon.

4.4 DATA AND INSTRUMENTATION

A year-long experiment recording underwater sound off the coast of Newport, Oregon, was conducted from March 2010 through April 2011 (Fig. 4.1; (Haxel *et al.*,

2011)) using a passive acoustic mooring located at 44° 41.8' N, 124° 08.9' W (YAQ-N) in 55 m water depth, 6 km from the coastline. The mooring was deployed on 20 March 2010, recovered 15 October 2010, redeployed 23 November 2010, and finally recovered 8 April 2011, providing the first nearly continuous, long-term acoustic recording in the shallow waters of the Pacific Northwest.

The passive acoustic mooring consists of an acoustic data logging system housed in a titanium pressure case and mounted on a weighted, semi-trawl protected aluminum frame 0.5 m above the seafloor. The hydrophone instrument is a low-power 16-bit data acquisition system and pre-amplifier using an omni-directional hydrophone from International Transducer Corporation (ITC1032) with sensitivity 192 dB $\mu\text{Pa V}^{-1}$ at 1 atm and 15°C. The system records continuously at a sample rate of 2 kHz, storing data to hard disks. Prior to analog-to-digital conversion, the signal is preconditioned by a pre-amplifier with a pre-whitening filter which helps de-emphasize the ambient noise spectrum below 20 Hz so that the 16-bit dynamic range can be fully utilized. The pre-amplifier consists of a series of gain stages with filters including two one-pole high-pass filters with cut-off frequencies at 1 Hz and 20 Hz respectively. The last stage of the pre-amplifier is an 8-pole elliptical anti-aliasing filter with a cut-off frequency (f_c) at 840 Hz and a stop band rejection ratio of -82 dB at $1.5 \times f_c$. Pre-amplifier gain increases within the pass-band from 15 dB at 1 Hz to 45 dB at 800 Hz. Prior to data analysis, the recorded signal is first converted to sound pressure relative to μPa by removing these instrument responses in the frequency domain. Calibration data is unavailable for the ITC1032 sensor at the temperatures (9-10°C), depth (~50 m) and frequency ranges (10-840 Hz) observed during the

experiment at the YAQ-N site. We therefore use the company-provided hydrophone sensitivity value ($-192 \text{ dB } \mu\text{Pa V}^{-1}$) and assume it remains constant within these temperature and frequency ranges. Furthermore, in order to avoid uncertainties associated with low frequency flow noise, this study focuses on spectral content at 10 Hz and above, limiting our analyses to the 10-840 Hz frequency band. Spectral estimates throughout this study are 2 sided and calculated from 1 second (2000 point) data blocks weighted with a Hanning taper and 0% overlap unless otherwise noted.

Neighboring coastal environmental conditions are measured and archived by the National Oceanic and Atmospheric Administration (NOAA) and Oregon State University's Hatfield Marine Science Center (HMSC) for correlation analysis with underwater acoustic recordings (Fig. 1). Hourly measurements of offshore significant wave heights (H_s), dominant wave periods (T_p), and coastal wind speeds (w_s) are provided through NOAA's National Data Buoy Center (NDBC, http://www.ndbc.noaa.gov/station_page.php?station=46050, http://www.ndbc.noaa.gov/station_page.php?station=nwpo3, 06/03/2012). Hourly rainfall rates (P) are calculated from 10-minute measurement intervals at the HMSC meteorological station (http://hmsc.oregonstate.edu/weatherproject/hmsc_weather.html, 06/03/2012). Additionally, records of fishing vessel traffic using the Port of Newport made available by the Oregon Department of Fish and Wildlife Marine Resources Program provide independent support for acoustic observations of ship noise at the YAQ-N receiver.

4.5 SOUND SOURCES

4.5.1 *Breaking surf*

In frequencies below 1 kHz, sounds generated by physical processes near the sea surface often control natural ambient noise levels. Similar to shallow water surf noise studies off California (Wilson *et al.*, 1997; Deane, 2000), the strongest and most persistent natural component of ambient sound energy observed at the YAQ-N site between 10 Hz - 100 Hz and within a few kilometers of the shoreline is noise generated by breaking surface waves in the shallow depths of the nearshore zone. With annual mean wave heights ($H_s = 2.62$ m) on the order of “heavy” surf conditions reported by (Wilson Jr *et al.*, 1985; Deane, 2000) for surf noise in central and southern California, the central Oregon coast represents a high-energy end member within the range of coastal waters affected by surf-generated noise. Figure 4.2 shows spectrograms and time series from the YAQ-N receiver in units of dB *re* 1 $\mu\text{Pa}^2\text{Hz}^{-1}$ and Volts, covering frequencies from 10-840 Hz during moderate surf conditions ($H_s = 2.74$ m). Pressure fluctuations resulting from waves breaking in the surf zone are recorded in groups of acoustic signals spanning the 10-840 Hz range and separated on time scales of several minutes (Fig. 4.2a & 4.2b). Group durations of 50–60 seconds are composed of quasi-periodic discrete increases in acoustic energy lasting up to five seconds associated with individual wave breaking (Fig. 4.2c & 4.2d).

Although surf-generated noise occurs across the recorded spectrum of the YAQ-N receiver, the majority of acoustic energy produced by breaking waves in the surf zone is concentrated at the infrasonic frequency range below $f < 20$ Hz. The conversion of mechanical energy from plunging wave breaking to acoustic energy in the surf zone

is initiated by a hydraulic shock emanating from the impact of the falling water mass which generates an intense low-frequency acoustic pulse at the seafloor referred to as “surfseism” (Saenger, 1961). The resultant intense low-frequency hydroacoustic energy reaching the YAQ-N receiver at infrasonic frequencies ($10 \text{ Hz} < f < 20 \text{ Hz}$, Fig. 4.2c) demonstrates the importance of surf noise as a natural contributor to the low frequency shallow water noise spectrum.

Surf noise energy levels have been shown to scale with incident wave heights and shore-directed wave energy flux within the surf zone on time scales of individual wave cycles (Deane, 2000). One-second spectral estimates averaged over 10-minute data intervals recorded during high ($H_s = 6.69 \text{ m}$), average ($H_s = 2.74 \text{ m}$), and low ($H_s = 0.66 \text{ m}$) energy conditions reveal an average increase of 15 dB from calm to energetic situations across the 10-840 frequency range. Furthermore, during high surf, ambient levels decrease from 120 dB to 83 dB in the 10–100 Hz band marking a 37 dB/decade reduction in acoustic energy as a function of increasing frequency, while sounds generated by moderate conditions, produce a 25 dB/decade decrease (97 dB to 72 dB) observed over the same frequency interval (10-100 Hz). In comparison, low frequency acoustic energy accompanying small incident wave energy conditions remains relatively stable, generating ambient levels varying between 72 – 79 dB within the same 10 – 100 Hz frequency band and lacking the decreasing trend toward higher frequencies observed in both the high and moderate wave energy conditions. The observed variability in spectral levels below $f < 100 \text{ Hz}$ associated with rising wave heights further illustrates the sensitivity of the low frequency component of the ambient noise spectrum to surf generated noise.

A long-term spectrogram displays the temporal variability in low frequency surf-generated noise observed at the YAQ-N mooring site (Fig. 4.4a). The spectrogram is composed from hourly averaged, spectral estimates calculated from 1-second blocks of data weighted with a Hanning taper and no overlap. Energy levels up to 100 Hz exhibit the frequency structure of the time averaged signal during a variety of wave height conditions, emphasizing the majority of energy concentrated in the infrasonic range ($10 \text{ Hz} < f < 20 \text{ Hz}$). The time series of hourly significant wave height (H_s) measurements at the NDBC 46050 buoy (Fig. 4.4b) also shows a noticeable seasonal increase in H_s associated with fall, winter and spring storms resulting in elevated surf generated noise levels. A scatter plot comparing acoustic power averaged across 10-20 Hz at one hour intervals with offshore significant wave height (H_s) buoy measurements (Fig. 4.4c) demonstrates the linear relationship between increasing wave heights and rising acoustic energy recorded in the surf generated noise band. Significant wave heights and surf noise are positively correlated ($r = 0.69$, $p \lll 0.001$) at 95 % confidence, showing the upward trend in acoustic energy accompanying building surf. Nevertheless, additional variability observed within the 10-20 Hz frequency band unrelated to breaking surf generated noise suggests contributions from alternative sound sources (e.g. vessels, baleen whales) also occasionally influence ambient levels within this low frequency range.

4.5.2 Flow noise

Total pressure fluctuations recorded by the hydrophone are the sum of acoustic (propagating) signals and nonacoustic energy associated with current flow near the

hydrophone surface (flow noise). In 55 m water depths, the bottom-moored hydrophone periodically encounters alternating hydrodynamic flows from large surface wave-induced orbital motions superimposed on smaller amplitude, mean low-frequency currents. Theoretical studies suggest the largest component of flow noise results from the advection of a pre-existing turbulent field past the hydrophone (Strasberg, 1979). Furthermore, modeled relationships between flow speed and ambient spectrum levels indicate a contamination velocity threshold of ~ 26 cm/s for frequencies 10 Hz and below. Unfortunately, without in-situ measurements of the turbulent velocity field near the YAQ-N hydrophone receiver, it is impossible to quantify the contribution of flow noise to the observed ambient sound levels below 10 Hz. Therefore, restricting our analysis to frequencies 10 Hz and above largely avoids flow noise contamination resulting from wave-induced flow experienced during extreme surf conditions.

4.5.3 Wind

The predominant mechanism for wind-generated noise in the ocean occurs through wind-induced wave breaking at the sea surface. As wind speeds increase, wind stress on the ocean surface becomes sufficient to produce short period wave breaking known as “whitecaps”. Bubbles created in the shallow surface layer from whitecaps undergo “breathing” mode oscillations radiating acoustic energy (Medwin and Beaky, 1989) that scales with wind speed (Vagle *et al.*, 1990) thus contributing to ambient noise levels above a few hundred Hz. Scatter plots of acoustic power averaged across two octave bands with center frequencies at 250 Hz and 500 Hz show

considerable variation with wind speeds (w_s) measured from the nearby coastal anemometer NWP03 station (Fig. 4.5a & 4.5b). Energy in the octave bands from Figures 4.5a & 4.5b is further processed into mean levels for $w_s = 10$ cm/s bins by taking the average of all acoustic energy values that lie within a given wind speed bin (Fig. 4.5c & 4.5d). Variations in bin-averaged values suggest for wind speeds less than 10 m/s, mean acoustic levels are not strongly influenced by wind speed. Meanwhile, at wind speeds above 10 m/s, bin averaged noise levels increase steadily with rising wind speeds. Limiting hourly observations to wind speeds $w_s \geq 10$ m/s, produces significant correlations ($r_{250\text{Hz}} = 0.34$, $p \ll 0.001$ and $r_{500\text{Hz}} = 0.37$, $p \ll 0.001$ at 95% confidence) with acoustic 250 Hz and 500 Hz octave band energies. The linear increasing trends in acoustic energy with the logarithm of wind speeds ≥ 10 m/s (Fig 4.5a & 4.5b) demonstrates the contribution of spatially integrated acoustic radiation from wind induced whitecaps occurring over a large area of ocean surface on ambient noise levels in the 250 Hz and 500 Hz octave bands at the YAQ-N receiver.

4.5.4 Rainfall

The physical mechanisms for sounds generated by rainfall in the oceans are well understood (Prosperetti and Oguz, 1993) with peaks in acoustic energy occurring in the 15–20 kHz range (Nystuen, 1986). Correlation analysis of ambient sound conditions at the YAQ-N station using 2 octave bands with center frequencies of 250 Hz and 500 Hz indicate spectral levels are uncorrelated ($r_{250\text{Hz}} = 0.003$, $p_{250\text{Hz}} = 0.90$ and $r_{500\text{Hz}} = 0.03$, $p_{500\text{Hz}} = 0.28$ at 95% CI) with nearby hourly rainfall measurements. The lack of a statistical connection between rainfall rates and ambient noise at

frequencies below 840 Hz suggests that leaking of energy down to lower frequencies are limited and the contribution of rain generated sound within the region is concentrated at frequencies higher than those measured in this study.

4.5.5 Biological sounds

Biological sources also make significant, although more transient contributions to the noise budget of the central Oregon coast. For instance, the seasonal migration of multiple species of Mysticeti (baleen) whales through the YAQ-N area is accompanied by an increase in acoustic energy at particular frequencies resulting from their vocalization behavior. This increase is temporally limited, lasting from a few hours to days at a time, and focused within species-specific frequency bands.

Vocalizations from a population of northeast Pacific blue whales (*Balaenoptera musculus*) recorded at YAQ-N receiver show the characteristic AB and ABBB song pattern (Fig. 4.6a; (Rivers, 1997). The A part of the call unit is pulsed with multiple time offset nonharmonic components, followed by the B unit, which is tonal including a series of higher-frequency harmonics. These vocalizations are among the loudest ($188 \text{ dB}_{\text{rms}}$ *re* $1 \mu\text{Pa}$ @ 1m) and lowest frequency (12 Hz – 100 Hz) sounds of any animal made on earth (Cummings and Thompson, 1971) and are the energetically dominant, biologically generated signal recorded at the YAQ-N receiver. Similarly, densely spaced fin whale (*Balaenoptera physalus*) vocalizations are also recorded on the YAQ-N hydrophone (Fig. 4.6b) on a seasonal basis. The low-frequency, downsweeping call is generally referred to as “the 20 Hz pulse” related to its center frequency (Watkins *et al.*, 1987). The humpback whales’ (*Megaptera novaeangliae*) complex songs (Tyack and Clark, 2000) consisting of whistles, whoops, moans, and

buzzes (Tyack, 1981) are also commonly observed during the fall season on the YAQ-N hydrophone receiver (Fig. 4.6c). The presence of each of these whale species within the acoustic dataset was visually identified by an analyst through spectrogram analysis. A time series showing an acoustic survey of hours containing whale vocalizations from blue, fin, and humpback whales (Fig. 4.6d) reveals the presence of these species beginning in early September and ending in early January. Vocalizations appear to peak from mid-October through November, although a gap in the data (16 October –22 November) prohibits the exact timing of maximum activity.

Although certain species of fish common to the region are known to transmit low-frequency acoustic energy generally below 1 kHz (Kasumyan, 2008), no fish sounds were observed within the data. Similarly, gray whale vocalizations could not be identified within the acoustic record despite their confirmed presence near the YAQ-N mooring during gray whale visual surveys from Yaquina Head in January 2011 (survey information courtesy of the Marine Mammal Institute, Oregon State University).

4.5.6 Ship noise

Ambient sound levels at the YAQ-N receiver are affected by mechanical noise generated by local vessel activities concentrated near the Port of Newport (10.5 km) as well as the nearly constant background acoustic energy radiated by distant commercial shipping. From supertankers on the outer shelf to small fishing vessels, ship generated noise can be identified from unique spectral characteristics of the acoustic energy radiated by the vessels' propulsion system, propeller blade noise and

cavitation, as well as the operation of winches, diesel engines, generators, and other shipboard equipment (Ross, 1976). The frequency-dependent nature of ship-born acoustic signals is related to the size of the vessel, the vessel speed, and the nature of the machinery generating the sound. Figure 4.7a shows a typical spectrogram from a moving vessel's rotating propeller blade noise during an hour of recording at the YAQ-N hydrophone station. Tones associated with the propulsion system of the ship vary in time as a result of the slight delay in arrivals associated with the direct and reflected surface paths of wide-band noise signals transmitted from the moving vessel to the fixed YAQ-N receiver (known as the frequency-dependent Lloyd mirror effect (Etter, 1991)). Propeller blade noise and other ship-based signals are visually identified in spectrograms by an analyst, and therefore likely reflect minimum values for ship noise occurrence over the year-long YAQ-N hydrophone deployment.

Locally generated ship noise observations are summarized in a time series of hourly percentages from each day containing vessel radiated noise contamination (Fig. 4.7b). Of the total 8169 observation hours, 66% contain visually detected ship noise with maximums occurring during summer months. Percentiles indicate, over the course of a year, 95% of days have at least one hour of detectable ship generated noise, while 10% of days are contaminated with ship-generated signals over the complete 24 hours. Visual survey data and logbooks of sport and commercial fishing vessel's transiting to and from the Port of Newport (Oregon Department of Fish and Wildlife Marine Resources Program) show similar trends (Fig. 4.7c). The increase in acoustically detected vessel activity during the summer months reflects a substantial rise in summer sport fishing traffic. Similar elevated occurrences of vessel noise

during winter months are attributed to the harvest operations of Newport's commercial crabbing fleet. A scatter plot comparing the 10-840 Hz band averaged acoustic power with the logarithm of combined sport and commercial vessel numbers shows an increase in ambient sound levels with increasing vessel activity (Fig. 4.7d). Vessel number data provided as weekly totals required the hourly averaged acoustic spectral levels to be further time averaged into weekly intervals. Cross correlation analysis between ambient noise levels and the number of vessels transiting to and from the Port of Newport yields a coefficient $\rho = 0.45$ with $\rho_c = 0.36$ @ 95% CI suggesting sounds radiated from sport and commercial vessels are important sources of anthropogenic noise at the YAQ-N station.

4.5.7 Comparison of sound sources

A plot of acoustic energy levels from characteristic sound sources recorded at the YAQ-N receiver summarizes the relative energy contributions from natural and anthropogenic sounds to the noise budget of the area within the 10-840 Hz frequency band (Fig. 4.8). The spectral energy curves in Figure 4.8 are composed from 10-minute time averages of 1-second spectral estimates. The “quiet” curve serves as the minimum noise level lacking any significant, observable signal contribution from natural or anthropogenic sources. Breaking surf and blue whale sound sources have a strong influence on ambient levels below 50 Hz, meanwhile the example of locally generated ship noise dominates spectral levels exceeding 50 Hz. The spectral curve associated with surf-generated noise was calculated during heavy surf and wind conditions ($H_s = 8.17$ m, $w_s = 10.1$ m/s) showing increases between 24-38 dB above “quiet” conditions in the 10-20 Hz surf noise band. The relative difference in acoustic

energy encountered during heavy weather (surf and wind) compared to background (quiet) conditions begins to decrease with frequencies beyond 20 Hz, reaching a minimum around 9 dB between 75-80 Hz. Spectral levels during high energy conditions then begin to gradually diverge from background conditions after 100 Hz, peaking at a difference of 30 dB in frequencies around 500 Hz resulting from wind induced whitecapping. Blue whale vocalizations recorded at the YAQ-N receiver show 15–45 dB increases in energy above “quiet” conditions occurring in discrete spectral bands associated with harmonics and other species call characteristics within the 10–100 Hz frequency range. Acoustic energy levels radiated from local vessels vary from 38-52 dB above “quiet” conditions across the 100-840 Hz frequency band, demonstrating the strong effect of anthropogenic sound sources on the noise budget and ambient sound levels of this coastal site.

4.6 AMBIENT NOISE ANALYSIS

4.6.1 Spectral Averages

Time averaged spectral estimates from continuous acoustic recordings provide important information on the frequency structure of received energy levels. Spectral levels calculated from 1-second, non-overlapped 2000 point data blocks weighted with a Hann taper are averaged over 200-second intervals, remaining consistent with the digital approach used by McDonald et al. (2008) and similar to Wenz's (1964) 200-second long 1/3 octave band averages from a shallow water site off San Clemente Island in Southern California. The 200-second long spectral averages from

YAQ-N span 342 recording days for a total of 147,100 time-averaged energy estimates.

Selected percentiles from the cumulative distribution of 200 second, time averaged spectral energy levels versus frequency over the year long record provide a basis for the local “noise budget” of the area (Fig. 4.9). Spectral energy levels generally decrease with higher-frequencies varying between 82 dB *re* 1 $\mu\text{Pa}^2/\text{Hz}$ at 10 Hz down to 72 dB *re* 1 $\mu\text{Pa}^2/\text{Hz}$ at 840 Hz. A rise in energy is observed from 15-28 Hz produced by the seasonal vocalization patterns of blue and fin whales. Another rise in ambient levels is observed in frequencies between 35 and 75 Hz, with a local maximum of 81 dB *re* 1 $\mu\text{Pa}^2/\text{Hz}$ occurring at 57 Hz. This rise in ambient levels is attributed to the persistent noise radiated by distant commercial shipping (Wenz, 1962; Andrew *et al.*, 2002; McDonald *et al.*, 2006). The notion this peak results from contamination by 60 Hz electronically generated system noise is dismissed, since this would generate a much sharper peak confined to a particular spectral band. Instead, a broad spectral increase in ambient levels is observed, peaking between 50 and 60 Hz, similar in frequency to ambient levels from deep ocean receivers that have been attributed to commercial shipping. The largest variations in energy between the 99th percentile and mean levels occur in frequencies below 100 Hz, reaching a maximum at 10 Hz where the 99th percentile exceeds mean values by 29 dB. This reflects the strong influence of surf noise, where infrequent instances of extreme wave heights raise acoustic energy levels well above mean values. The 1 percentile shows the largest divergence below mean energy values (17 dB) occurring in frequencies above 100 Hz.

A comparison of average spectral energy levels from the present study with levels reported from recent recordings at two sites in deep, northeast Pacific open ocean waters (Andrew *et al.*, 2002; McDonald *et al.*, 2006) is shown in Figure 4.10a. Attenuation of low frequency acoustic energy resulting from seafloor interactions in the shallow continental slope waters surrounding the YAQ-N receiver produces average spectral levels up to 15 dB below those observed at the deep ocean stations. Meanwhile, at frequencies above ~60 Hz for San Nicolas and ~150 Hz for Point Sur, YAQ-N ambient levels rise above deep water spectral values resulting from the increased propagation efficiency of higher frequency energy in the shallow waters of the YAQ-N site.

Examples comparing YAQ-N ambient levels during heavy surf conditions ($H_s = 8.17$ m , $w_s = 10.1$ m/s) with recordings made in the 1940's off the coast of Fort Lauderdale, Florida in 200 m depths at sea state 5 (Knudsen *et al.*, 1948), the 1960's from 50 m water depths on the Scotian shelf during average wind speeds of 15 m/s (Piggott, 1964) and in the 1980's from 30-90 m water depths during "heavy" surf conditions ($H_s = 2.55$ m) near Monterey Bay, California (Wilson Jr *et al.*, 1985) are shown in Figure 4.10b. The spectral curves from these high-energy environmental conditions spanning nearly 70 years in a variety of shallow water coastal settings are remarkably consistent at around 80 dB *re* 1 $\mu\text{Pa}^2/\text{Hz}$ for frequencies ranging from 100-800 Hz. As previously shown (section 4.5.1), for frequencies below $f < 100$ Hz, ambient levels from the YAQ-N receiver increase rapidly with decreasing frequency in the surf generated noise band. Acoustic energy levels from the YAQ-N recordings are elevated from those reported by Wilson Jr. et al. (1985) in California resulting

from the difference in “heavy” surf conditions experienced at each site. The increased ambient levels during extreme wave height conditions emphasize the Pacific Northwest coastline as a high-energy end member of the surf noise spectrum.

A “floor” spectrum, defined as the lowest one percentile from the cumulative distribution of time-averaged spectral levels, has been used to characterize ambient noise in the absence of natural or anthropogenic sources (McDonald *et al.*, 2008). The presumed floor spectrum or minimum noise level for the YAQ-N site is shown by the one percentile spectral curve in Figure 4.11. The peak in noise floor ambient levels (40-100Hz) is attributed to the distant sound energy radiated by commercial shipping traffic beyond the outer continental shelf. Noise floor spectral levels can potentially be used to evaluate the contribution of anthropogenic sources above “quiet” ambient conditions.

4.6.2 Total sound pressure levels

A quantitative summary measure of acoustic energy known as sound pressure level (SPL, force per unit area) is often used as a method for representing the broadband time-varying acoustic energy levels at a receiver. SPL reported in dB *re* 1 μ Pa is defined as:

$$\text{SPL (dB re 1 } \mu\text{Pa)} = 20 \log_{10} \left(\frac{p_{rms}}{p_{ref}} \right) \quad (4.1)$$

where p_{rms} represents the root mean square of the pressure-corrected time series from the hydrophone, and the standard hydroacoustic reference pressure p_{ref} is equal to 1 μ Pa. Prior to SPL calculations, 1-second blocks are Fourier transformed into the frequency domain, corrected for hydrophone system response, and then inverse

Fourier transformed back into the time domain. Data are then band-pass filtered using 4th order Butterworth filters producing five octave band time series (center frequencies $f_c = 31.6$ Hz, 63.1 Hz, 125.9 Hz, 251.2 Hz and 501.2 Hz) in addition to the 10-840 Hz signal. One-second root mean square (*rms*) values of SPL are calculated and combined to form SPL_{rms} time series for each of these frequency bands.

A plot of weekly SPL_{rms} averages illustrates the time-dependent variability of the 10-840 Hz signal and octave bands (Fig. 4.12a). The strong influence of locally generated ship noise on sound pressure levels is evident through increasing trends in SPL_{rms} leading toward summer months, peaking in August with extreme vessel traffic activity (Fig. 4.12b). Meanwhile the impact of surf-generated noise on sound pressure levels (10-840 Hz) is less obvious, indicated by the sustained rise in significant wave heights near the end of September (Fig. 4.12c) coinciding with elevated SPL_{rms} values despite a substantial drop in vessel activity. Selected percentiles from the distribution of nearly 30 million, one-second SPL_{rms} values (10-840 Hz) are provided in Table 4.I with units of dB *re* 1 μ Pa. Minimum and mean SPL_{rms} levels for the year (10-840 Hz) reach 84 dB and 101 dB respectively, while energy radiated from a local vessel generates the maximum rms sound pressure level (152 dB). Percentiles from these distributions also identify the $f_c = 32$ Hz octave band as the least energetic, while the $f_c = 250$ Hz octave band most often contains the highest sound pressure levels.

4.7 DISCUSSION

Future human development of natural resources along the inner continental shelf of the Pacific Northwest coast is likely to increase ambient sound levels. Permitting

agencies and regulators (e.g., National Marine Fisheries Service [NMFS] and Oregon Department of Fish and Wildlife) use acoustic exposure criteria to limit behavioral disturbances and injury to fish and marine mammal species often based on sound pressure levels (SPL; (National Research Council, 2005)). NMFS currently uses an SPL threshold of 120 dB *re* 1 μ Pa (*rms*) for the onset of Level B harassment (behavioral disturbance) from continuous sound sources, and a Level B threshold of 160 dB *re* 1 μ Pa (*rms*) for pulsed sound sources. Threshold onset criteria of Level A harassment (animal injury) occurs at 180 dB *re* 1 μ Pa (*rms*).

Selected percentiles from the year-long distribution of 10-840 Hz one-second SPL_{rms} values recorded at the YAQ-N receiver show energy levels seldom exceed Level B harassment threshold criteria for continuous sounds (120 dB *re* 1 μ Pa; Table 4.1). Despite the measured maximum value of 152 dB, less than 1% of the nearly 30 million one-second SPL_{rms} measurements surpass the 117 dB level as indicated by the 99th percentile. Nevertheless, the frequency-dependent and seasonal nature of SPL_{rms} levels for this shallow coastal site suggest frequency weighting of SPL and sound exposure level (SEL) calculations (Southall *et al.*, 2007) may provide valuable information for evaluating the potential exceedance of critical threshold values associated with future human development in this marine ecosystem.

4.8 CONCLUSIONS

A continuous, year-long acoustic record (10-840 Hz) and selected percentiles from the cumulative distribution of spectral levels at the YAQ-N receiver provide a quantitative description of the frequency structure and acoustic energy levels

characteristic of this shallow water central Oregon coast area. Locally generated ship noise is a dominant and persistent feature of the acoustic spectrum in frequencies above 50 Hz, while nearly continuous noise radiating from distant commercial shipping produces a spectral peak in received levels between 50 and 60 Hz. The sounds generated by breaking surf at the coastline largely influence the spectrum below 100 Hz. A comparison of ambient levels from the YAQ-N receiver with acoustic energy recorded at similar shallow water sites during energetic environmental conditions emphasizes this Oregon coast site as a high energy end member within the range of shallow water areas influenced by breaking surf noise. Sounds generated by wind-induced wave breaking at the surface make significant contributions to ambient levels in the 250 Hz and 500 Hz octave bands for wind speeds greater than 10 m/s, while biological sound sources are more transient and associated with the migrations of large baleen whales peaking in the fall months and confined to particular frequency bands. The characterization of sound sources and spectral measurements of ambient levels in the 10-840 Hz frequency range from a variety of environmental and anthropogenic conditions presented in this study provides initial baseline information required for future noise comparisons related to human resource development along the central Oregon coast inner continental shelf region.

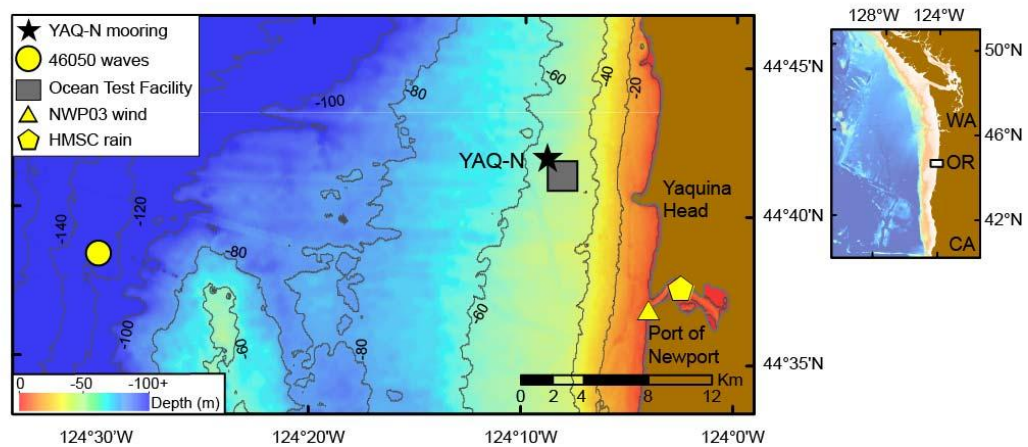


Figure 4.1 Instrument locations and local bathymetry surrounding the YAQ-N hydrophone receiver (left), and a regional map of the Pacific Northwest coast showing the location of the study (right). The acoustic mooring (YAQ-N) is identified by a star, the wave measurement buoy (NDBC #46050) is shown as a circle, the Northwest National Marine Renewable Energy Center Ocean Test Facility (OTF) for wave energy conversion devices is shown with a square, the anemometer station (NDBC #NWP03) is indicated with a triangle and the rain gauge instrument (Oregon State University) is shown with a pentagon. Bathymetry contour line depths are in meters.

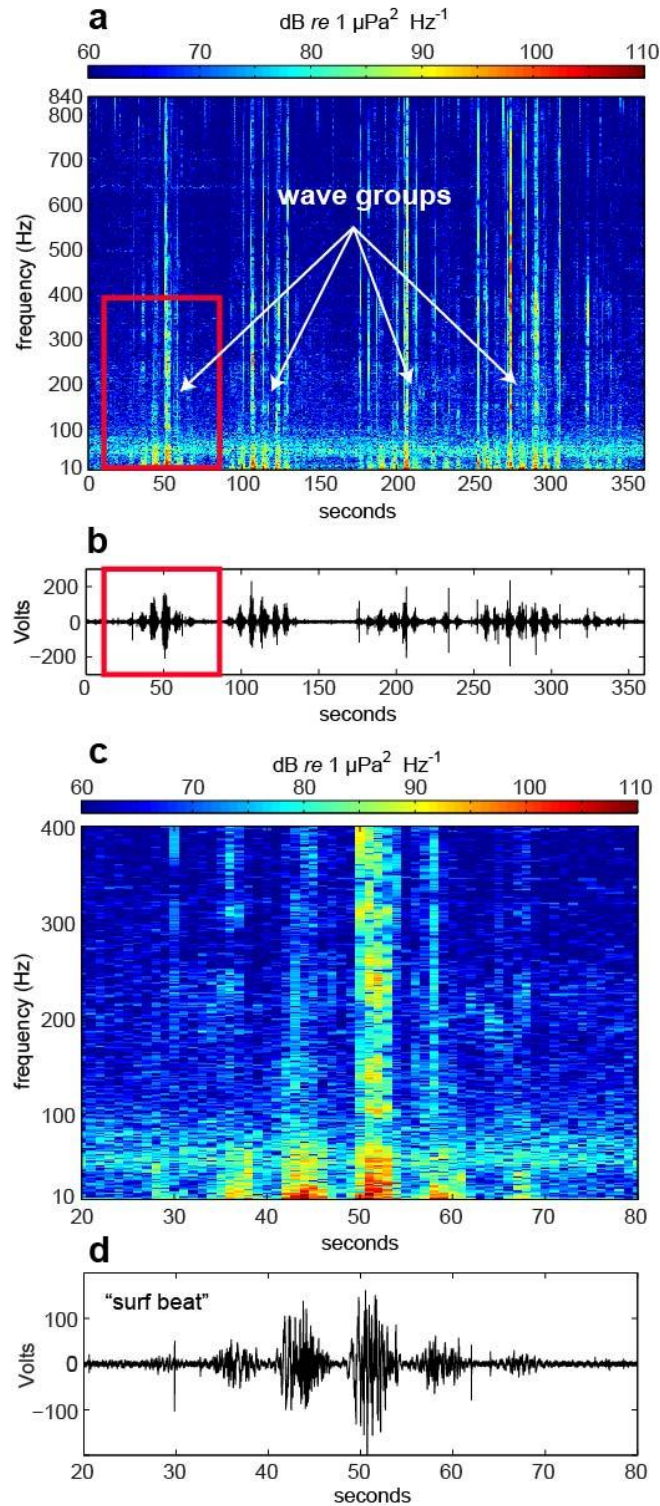


Figure 4.2 Spectrograms and time series showing acoustic arrivals of wave groups (a&b) from the YAQ-N mooring during a period of average wave heights $H_s = 2.74$ m. A zoomed view of a single wave group (20 to 80 seconds in a&b) reveals the acoustic signal generated by individual wave breaking known as “surf beat” (c&d).

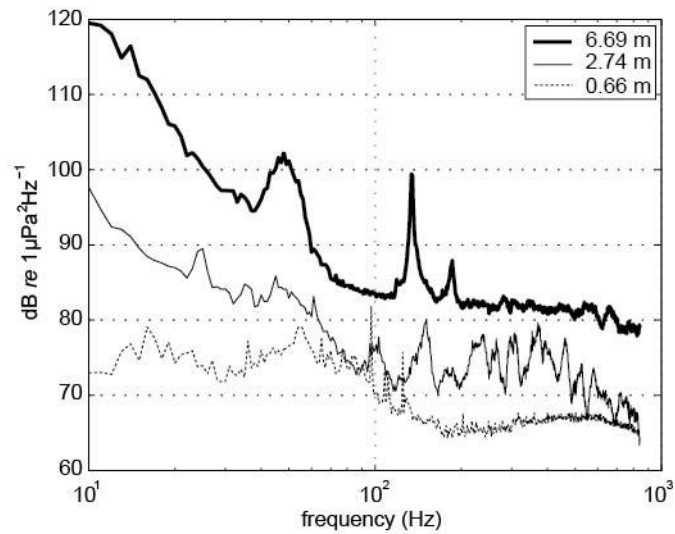


Figure 4.3. Spectral levels from 10-minute averages during periods of high ($H_s = 6.69$ m), average ($H_s = 2.74$ m), and low ($H_s = 0.66$ m) surf conditions. The horizontal frequency axis is shown in log scale to emphasize the strong increase in energy associated with lower frequency, ($f < 100$ Hz) surf generated noise.

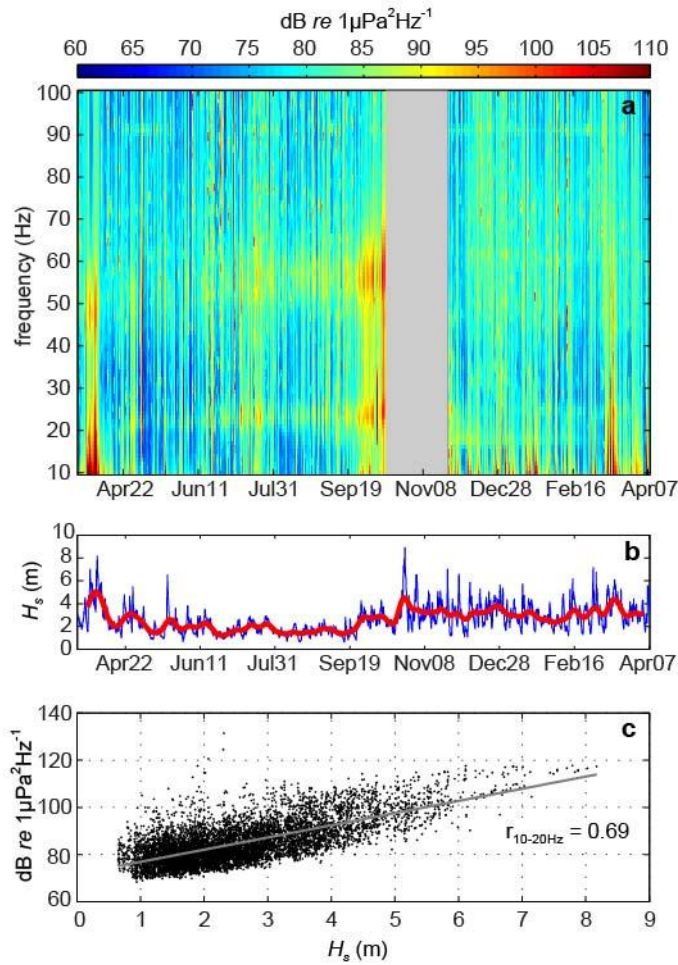


Figure 4.4. (a) A long-term spectrogram ($f < 100$ Hz) from the YAQ-N mooring site during the deployment year March 2010 – April 2011 emphasizes the seasonal dependence of surf-generated noise. A gray box separating the continuous spectra (October 16 - November 22) denotes a gap in recording. (b) Hourly H_s measured by the nearby NDBC 46060 buoy. A thick line shows the low-pass filtered (2 week Hanning window) H_s time series. (c) Scatter plot of the surf band-averaged noise levels ($10 \text{ Hz} < f < 20 \text{ Hz}$) versus significant wave heights (H_s) showing a linear upward trend with increasing incident wave energy, $r_{10-20\text{Hz}} = 0.69$.

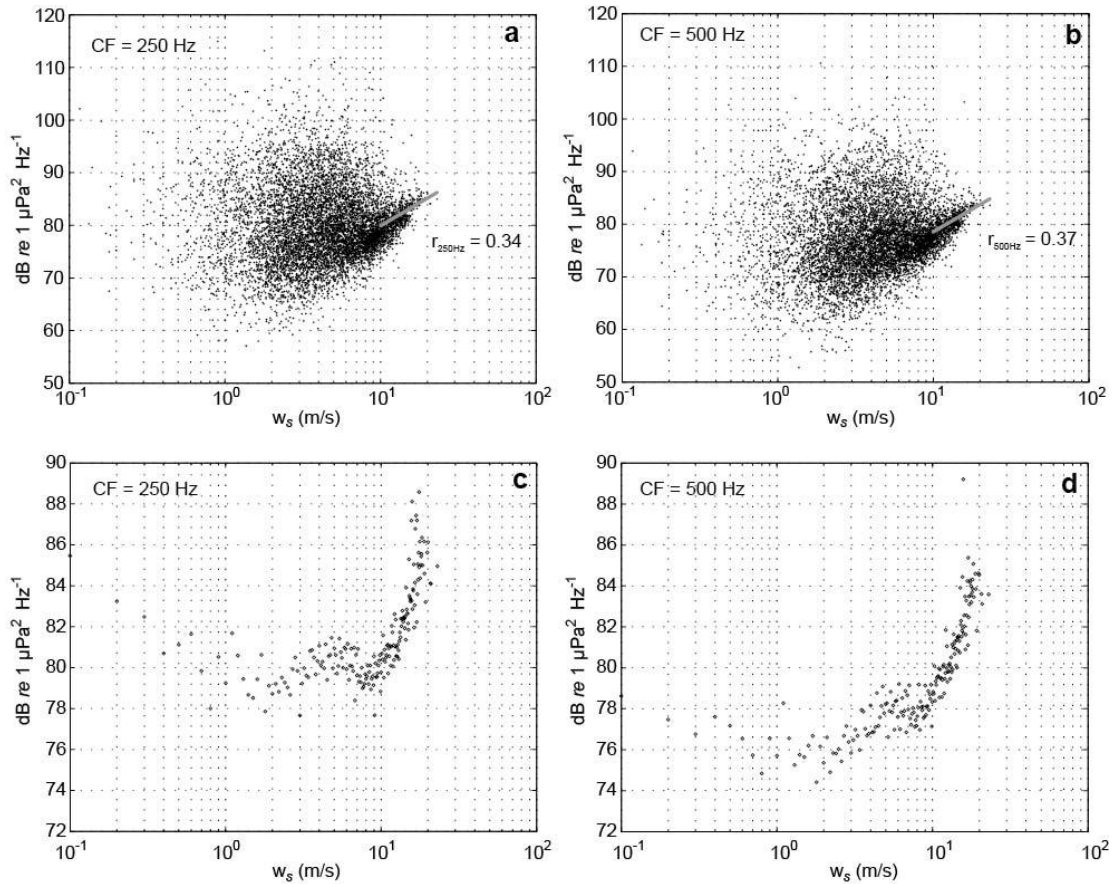


Figure 4.5 (a&b) Scatter plots of octave band-averaged ($f_c = 250 \text{ Hz}$, $f_c = 500 \text{ Hz}$) noise levels versus wind speeds (w_s). Ambient levels scale with the logarithm of wind speeds for $w_s \geq 10 \text{ m/s}$, with $r_{250\text{Hz}} = 0.34$ and $r_{500\text{Hz}} = 0.37$. (c&d) Mean noise levels calculated by dividing the wind speed axis in a&b into 10 cm/s bins and averaging the points that lie within each bin. For both octave bands, ambient noise levels begin to steadily increase as wind speeds reach $w_s \geq 10 \text{ m/s}$.

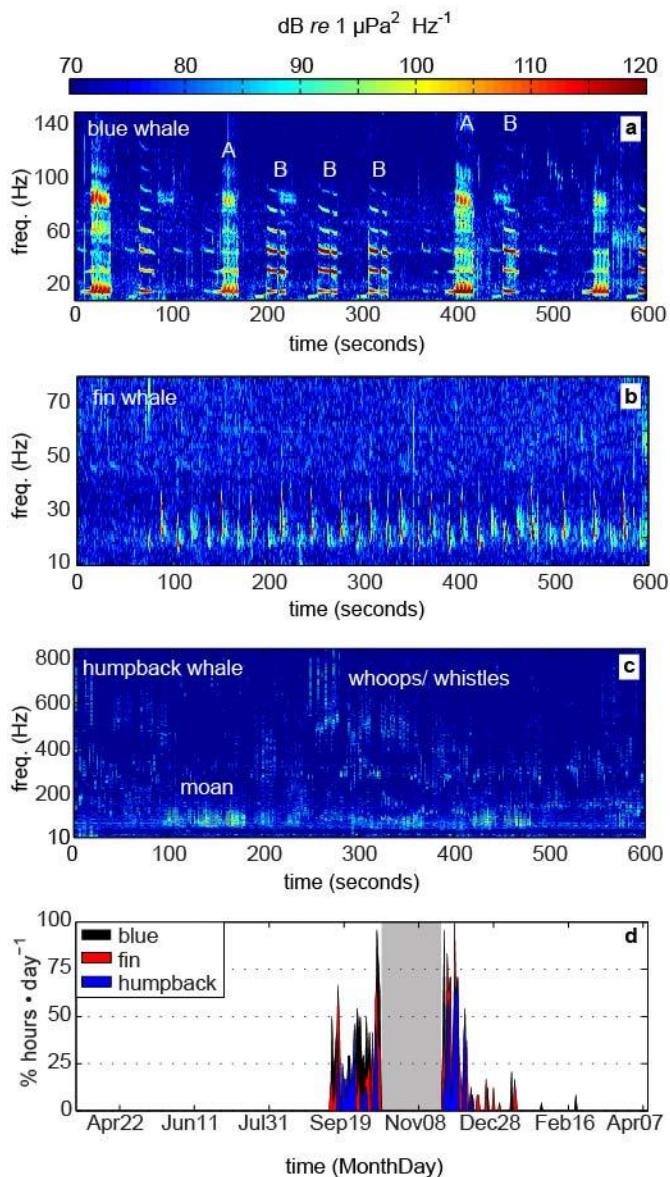


Figure 4.6 Spectrograms of vocalizations from a northeast Pacific blue whale (a), fin whale (b), and humpback whale (c) recorded by the YAQ-N receiver. A time series of the percentage of hours within a day where each type of whale call was observed (d), shows the acoustic presence of each species.

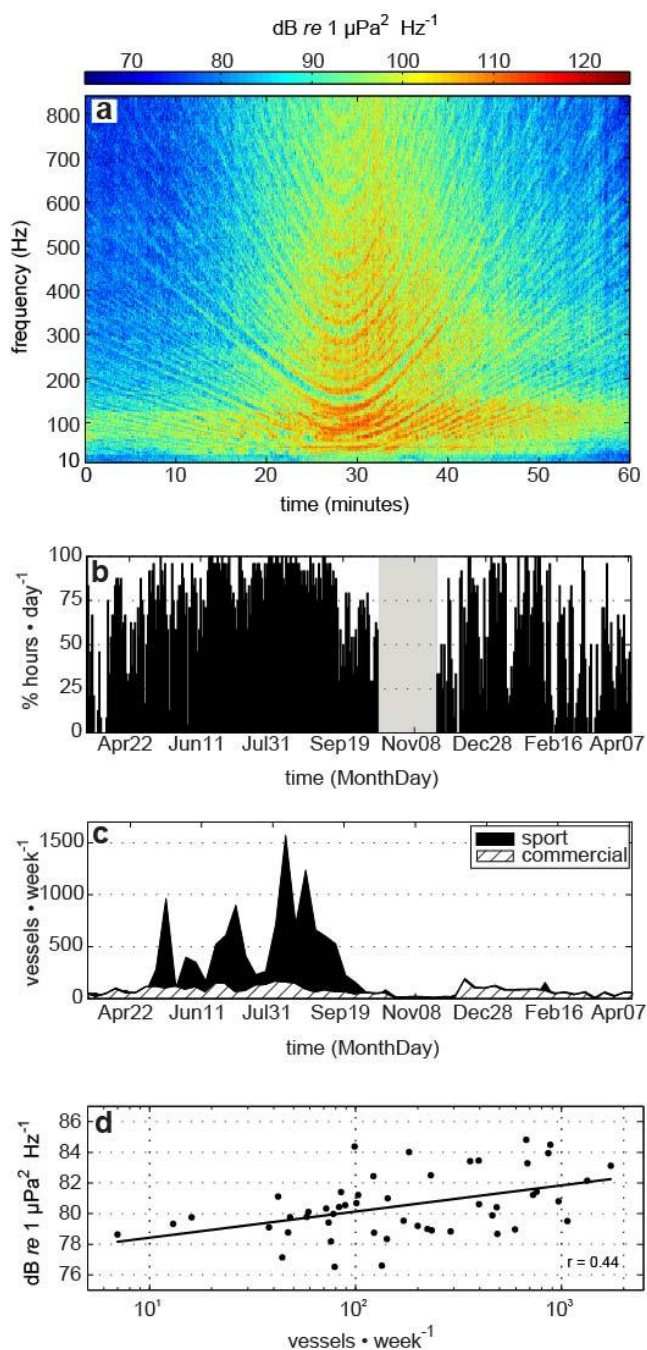


Figure 4.7 (a) An hour-long spectrogram showing the typical frequency structure of acoustic energy radiated from a moving ship near the YAQ-N receiver. (b) A histogram of the percentage of hours within a day where ship noise was acoustically detected at the YAQ-N receiver by an analyst. The grey box indicates a gap in the recording (October 16 - November 22). (c) Weekly counts of sport and commercial vessel traffic using the Port of Newport (data courtesy of ODFW, Marine Resources Program). (d) Scatter plot of the 10-840 Hz weekly averaged noise levels versus the logarithm of vessels transiting through the Port of Newport showing an upward trend with increasing vessel traffic, $r = 0.44$.

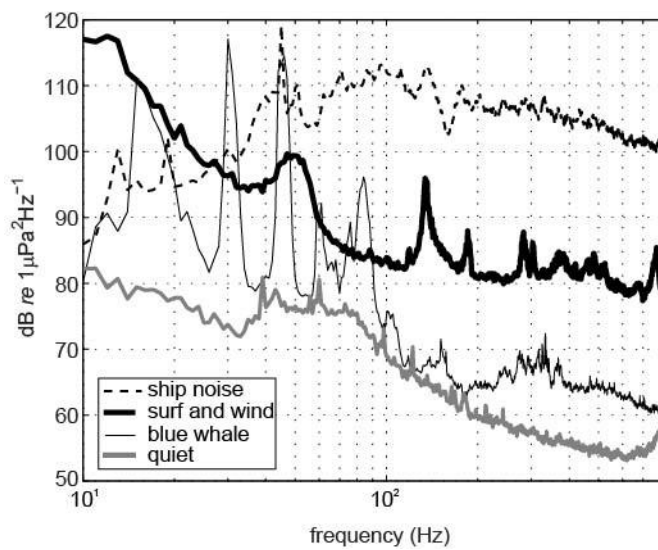


Figure 4.8 A summary comparison of relative acoustic energy levels associated with important sound sources recorded by the YAQ-N receiver. Spectral levels are averaged over 10 minute data intervals devoid of any significant, observable contamination from other sources.

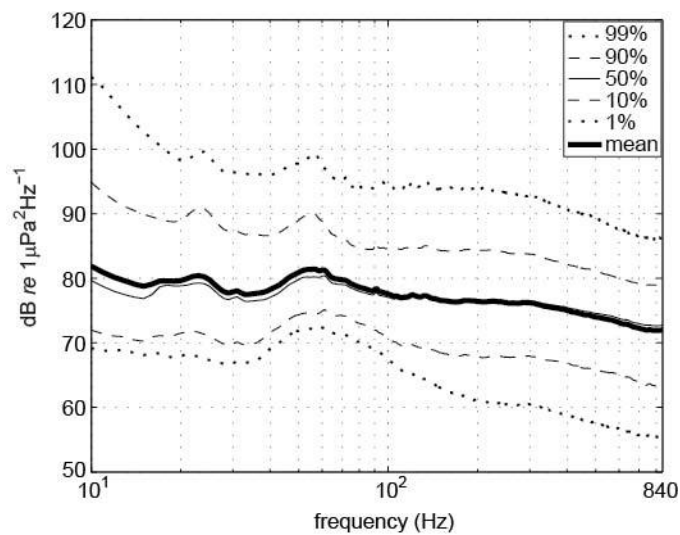


Figure 4.9 Selected percentiles from the cumulative distribution of spectral energy levels recorded by the YAQ-N receiver from March 2010 – April 2011. Spectral energy is averaged over 200 second intervals for a total of 147,100 spectra spanning 342 days.

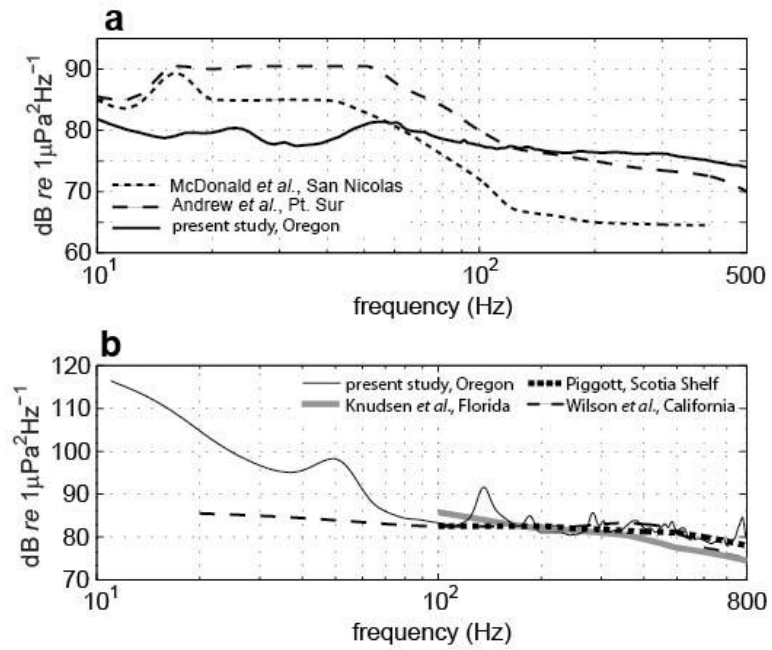


Figure 4.10 (a) Average spectral levels from the present study plotted with data reported in 2 recent studies from deep water stations in the NE Pacific for comparison between deep and shallow water ambient levels. (b) Spectral levels from the present study during high energy conditions ($H_s = 8.17$ m ; $w_s = 10.1$ m/s) plotted for comparison with similar shallow water high energy conditions in other coastal areas.

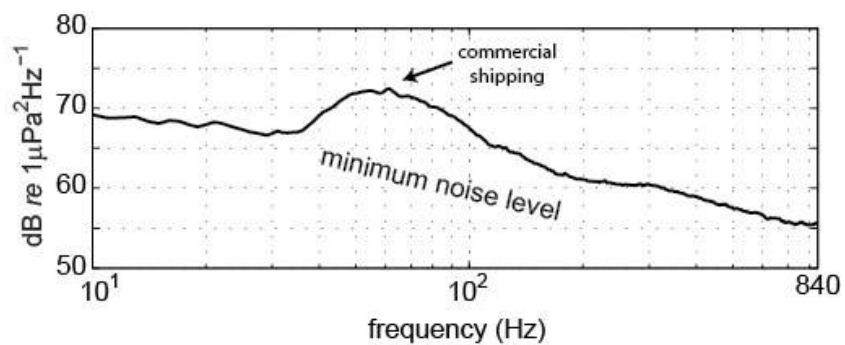


Figure 4.11 The 1 percentile curve from the cumulative distribution of time averaged spectral levels used to represent the noise floor for the YAQ-N receiver. Persistent noise radiated from distant shipping commerce makes a significant contribution to minimum noise levels.

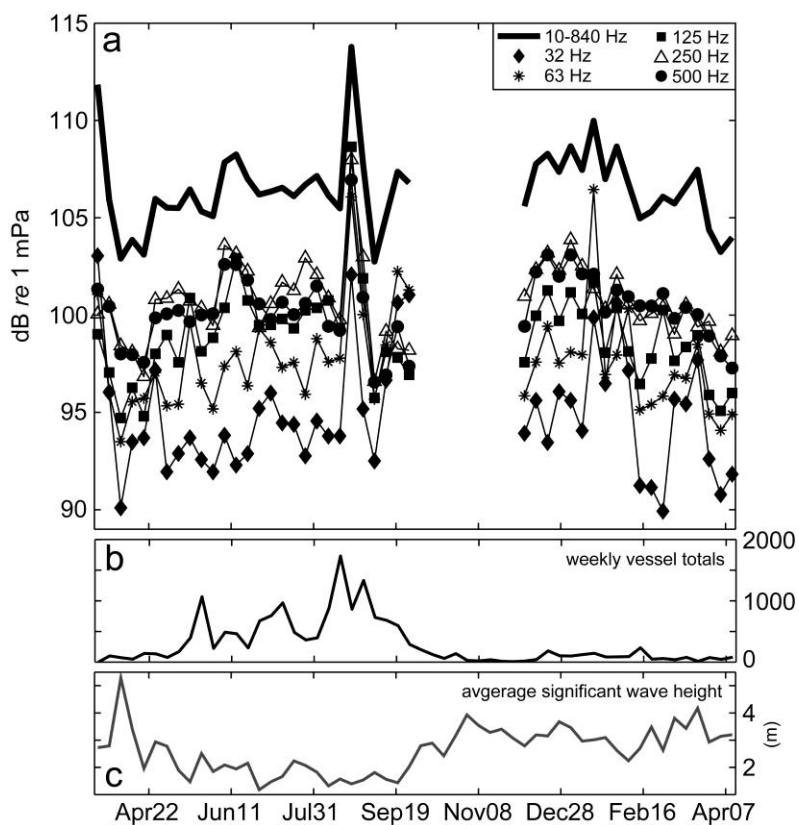


Figure 4.12 (a) Weekly averaged SPL_{rms} calculated from 1 second data intervals for the 10-840 Hz and 5 octave bands identified by center frequencies. (b) Weekly averaged significant wave heights (H_s) and (c) total numbers of sport and commercial vessels transiting through the port of Newport.

TABLE 4.1 Select percentiles from the distribution of one-second root mean square sound pressure levels (SPL_{rms}). Octave bands are identified by center frequencies with SPL_{rms} reported in dB *re* 1 μ Pa.

Center Frequencies (Hz)	Mean (dB)	Max (dB)	Min (dB)	99% (dB)	90% (dB)	50% (dB)	10% (dB)	1% (dB)
10-840	101	152	84	117	108	101	94	89
32	88	147	75	107	96	87	82	79
63	92	150	79	109	99	92	87	84
125	93	145	76	109	101	93	86	81
250	95	144	72	111	102	95	86	79
500	95	143	72	110	102	96	87	78

4.9 REFERENCES

- Andrew, R. K., Howe, B. M., Mercer, J. A., and Dzieciuch, M. A., 2002, Ocean ambient sound: comparing the 1960s with the 1990s for a receiver off the California coast: *Acoustics Research Letters Online*, v. 3, no. 2, p. 65-70.
- Au, W. W. L., 1993, *The sonar of dolphins*, (Springer-Verlag, New York Inc.), p. 277.
- Bassett, C., Thomson, J., Polagye, B., and Rhinefrank, K., 2011, Underwater noise measurements of a 1/7th scale wave energy converter, In Proceedings of MTS/IEEE OCEANS. Kona, USA. September 2011, p. 1-6.
- Chapman, N. R., and Price, A., 2011, Low frequency deep ocean ambient noise trend in the Northeast Pacific Ocean: *The Journal of the Acoustical Society of America*, v. 129, no. 5, p. EL161-EL165.
- Clark, C. W., Ellison, W. T., Southall, B. L., Hatch, L., Van Parijs, S. M., Frankel, A., and Ponirakis, D., 2009, Acoustic masking in marine ecosystems: intuitions, analysis, and implication: *Marine Ecology Progress Series*, v. 395, p. 201-222.
- Cummings, W. C., and Thompson, P. O., 1971, Underwater sounds from the blue whale, *Balaenoptera musculus*: *The Journal of the Acoustical Society of America*, v. 50, p. 1193.
- Deane, G. B., 2000, Long time-base observations of surf noise: *The Journal of the Acoustical Society of America*, v. 107, no. 2, p. 758-770.
- Edds-Walton, P. L., 1997, Acoustic communication signals of mysticete whales: *Bioacoustics*, v. 8, no. 1&2, p. 47-60.
- Etter, P.C., 1991, "Underwater acoustic modelling", Elsevier Sci. Pub. LTD, pp. 52-54.
- Haxel, J. H., Dziak, R. P., and Matsumoto, H., 2011, Obtaining baseline measurements of ocean ambient sound at a mobile test berth site for wave energy conversion off the central Oregon coast, In Proceedings of MTS/IEEE OCEANS. Kona, USA. September 2011, p. 1-5.
- Herzing, D. L., and Mate, B. R., 1984, Gray whale (*Eschrichtius robustus*) migrations along the Oregon coast, In *The Gray Whale, Eschrichtius Robustus*, edited by J. S. L. M.L. Jones, and S.L. Swartz (Academic Press Inc., New York), pp. 289-307.
- Hildebrand, J. A., 2009, Anthropogenic and natural sources of ambient noise in the ocean: *Marine Ecology-Progress Series*, v. 395, p. 5-20.

- Kasumyan, A. O., 2008, Sounds and sound production in fishes: *Journal of Ichthyology*, v. 48, no. 11, p. 981-1030.
- Knudsen, V. O., Alford, R., and Emling, J., 1948, Underwater ambient noise: *Journal of Marine Research*, v. 7, no. 3, p. 410-429.
- McDonald, M. A., Hildebrand, J. A., and Wiggins, S. M., 2006, Increases in deep ocean ambient noise in the northeast Pacific west of San Nicolas Island, California: *The Journal of the Acoustical Society of America*, v. 120, no. 2, p. 711-718.
- McDonald, M. A., Hildebrand, J. A., Wiggins, S. M., and Ross, D., 2008, A 50 year comparison of ambient ocean noise near San Clemente Island: A bathymetrically complex coastal region off Southern California: *The Journal of the Acoustical Society of America*, v. 124, p. 1985-1992.
- Medwin, H., and Beaky, M. M., 1989, Bubble sources of the Knudsen sea noise spectra: *The Journal of the Acoustical Society of America*, v. 86, p. 1124-1130.
- NRC (National Research Council), 2005, *Marine Mammal Populations and Ocean Noise: Determining When Noise Causes Biologically Significant Effects*. (National Academy Press), p. 126.
- Nystuen, J. A., 1986, Rainfall measurements using underwater ambient noise: *The Journal of the Acoustical Society of America*, v. 79, p. 972-982.
- Picciulin, M., Sebastianutto, L., Codarin, A., Farina, A., and Ferrero, E. A., 2010, In situ behavioural responses to boat noise exposure of *Gobius cruentatus* and *Chromis chromis* living in a Marine Protected Area: *Journal of Experimental Marine Biology and Ecology*, v. 386, no. 1, p. 125-132.
- Piggott, C., 1964, Ambient sea noise at low frequencies in shallow water of the Scotian Shelf: *The Journal of the Acoustical Society of America*, v. 36, no. 11, p. 2152-2163.
- Prosperetti, A., and Oguz, H. N., 1993, The impact of drops on liquid surfaces and the underwater noise of rain: *Annual review of fluid mechanics*, v. 25, no. 1, p. 577-602.
- Rivers, J. A., 1997, Blue whale, *Balaenoptera musculus*, vocalizations from the waters off central California: *Marine Mammal Science*, v. 13, no. 2, p. 186-195.
- Ross, D., 1976, Mechanics of underwater sound, *Mechanics of Underwater Noise* (Pergamon Press, New York), p. 375.

- Saenger, R. A., 1961, An estimate of the offshore ambient noise spectrum produced by pounding surf: *The Journal of the Acoustical Society of America*, v. 33, p. 1674.
- Simpson, S. D., Meekan, M., Montgomery, J., McCauley, R., and Jeffs, A., 2005, Homeward sound: *Science*, v. 308, no. 5719, p. 221-221.
- Southall, B., Bowles, A., Ellison, W., Finneran, J., Gentry, R., Greene, C., Kastak, D., Ketten, D., Miller, J., and Nachtigall, P., 2007, Marine mammal noise exposure criteria: Initial scientific recommendations," *Aquatic Mammals*, 33, 411-521.
- Strasberg, M., 1979, Nonacoustic noise interference in measurements of infrasonic ambient noise: *The Journal of the Acoustical Society of America*, v. 66, p. 1487-1493.
- Tyack, P., 1981, Interactions between singing Hawaiian humpback whales and conspecifics nearby: *Behavioral Ecology and Sociobiology*, v. 8, no. 2, p. 105-116.
- Tyack, P. L., and Clark, C. W., 2000, Communication and acoustic behavior of dolphins and whales: In *Hearing by Whales and Dolphins*, edited by Au, W.L., Popper, A.N., and Fay, R.R., Springer Handbook of Auditory Research Series 12, p. 156-224.
- Vagle, S., Large, W. G., and Farmer, D. M., 1990, An evaluation of the WOTAN technique of inferring oceanic winds from underwater ambient sound: *Journal of Atmospheric and Oceanic Technology*, v. 7, p. 576-595.
- Watkins, W. A., Tyack, P., Moore, K. E., and Bird, J. E., 1987, The 20-Hz signals of finback whales (*Balaenoptera physalus*): *The Journal of the Acoustical Society of America*, v. 82, no. 6, p. 1901-1912.
- Wenz, G. M., 1962, Acoustic ambient noise in the ocean: spectra and sources: *The Journal of the Acoustical Society of America*, v. 34, p. 1936.
- , 1964, Ambient noise measurements west of San Clemente Island, U.S. Navy Electronics Laboratory Report 1235, p. 46.
- Wilson Jr, O., Wolf, S. N., and Ingenito, F., 1985, Measurements of acoustic ambient noise in shallow water due to breaking surf: *The Journal of the Acoustical Society of America*, v. 78, p. 190-195.
- Wilson, O. B., Stewart, M. S., Wilson, J. H., and Bourke, R. H., 1997, Noise source level density due to surf. I. Monterey Bay, CA: *IEEE Journal of Oceanic Engineering*, v. 22, no. 3, p. 425-433.

Wladichuk, J. L., Megill, W. M., and Blondel, P., 2008, Passive acoustic localization techniques of Eastern Pacific grey whales: *The Journal of the Acoustical Society of America*, v. 123, no. 5, p. 3207.

Wright, A. J., Soto, N. A., Baldwin, A. L., Bateson, M., Beale, C. M., Clark, C., Deak, T., Edwards, E. F., Fernández, A., and Godinho, A., 2007, Do marine mammals experience stress related to anthropogenic noise?: *International Journal of Comparative Psychology*, v. 20, no. 2.

5 SUMMARY

A broad range of underwater acoustic methods are commonly used in commercial, industrial, scientific and societal applications across the world's oceans. For example, marine acoustic systems and technologies are essential for vessel navigation and safety instrumentation, locating and targeting marine species for harvest, military applications, seafloor mapping, energy resource exploration and more recently, the environmental management of sensitive ecosystems and habitats. This dissertation takes advantage of a diverse range of advanced acoustic techniques used to produce earthquake catalogs (*T*-phase & OBH) based on acoustic propagation of seismic energy in the deep ocean environments of the northeast Pacific. Furthermore, passive hydrophone technology and acoustic methods are used to measure and characterize ambient noise levels and the energy contribution of sound sources along an area of the inner continental shelf.

In Chapter 2, an acoustically derived regional earthquake catalog provides an improved picture of seismic activity along the remote seafloor spreading ridge and transform boundaries of the Juan de Fuca plate system in the northeast Pacific. First order statistical analysis reveals a fundamental difference in the temporal distribution of earthquakes along ridges and transform faults in the region. Seismicity rate distributions along ridge segments are highly skewed indicating earthquakes occur in brief, intense episodes associated with magmatic intrusions and lack significant background seismicity. Meanwhile, transform fault zone earthquake rate distributions exhibit substantial background seismicity and are more reflective of steady plate

motion, punctuated with short, less severe increases in seismic activity. Segment scale EOF analysis identifies and quantifies the dominant patterns or modes of earthquake rate variability within the catalog. Eigenvalues trend toward increasing levels for EOFs associated with ridge segments, whereas transform fault zones tend to produce modes with similar, lower eigenvalues. Further analysis indicate a significant 3-year rise in earthquake activity levels observed along both ridge and transform segments of the Juan de Fuca system following the 1998 dike intrusion and eruption at Axial Seamount suggesting a plate scale change in seismic energy release over that period.

Results from the regional hydrophone earthquake catalog analysis in Chapter 2 reveal seismicity associated with the 1998 magmatic event at Axial Seamount produced the single largest earthquake rate change over the ten-year study (1991-2002). In Chapter 3, acoustic records from an ocean bottom hydrophone (OBH) array located at Axial provide a multi-year time series of micro-seismicity leading toward a subsequent magmatic intrusion in April 2011. Local micro-seismicity rates are observed to begin increasing within roughly 2 years of the intrusion in 2011. This result is consistent with previously observed increases prior to the eruption in 1998 suggesting this rate change may be a useful tool for future event forecasting. Although episodic increases in micro-seismic activity levels are not accompanied by significant seafloor geodetic signals, longer interval trends (e.g. months) in both seismic energy and caldera inflation are observed within 2 years prior to the 2011 intrusion. This observation suggests a brittle crustal response to increasing magma pressures on the shorter time scales associated with seismic swarms while ductile crustal deformation occurs over longer time periods in conjunction with increasing

crustal elasticity prior to eruption. Results from this study provide potentially important forecasting information for the next intrusion event in the context of instrument preparation and sampling strategies for the recently installed Ocean Observatories Initiative (OOI) regional node at Axial Seamount.

In Chapter 4, analysis of a yearlong acoustic record from a passive seafloor hydrophone mooring located in the shallow coastal waters off central Oregon in the northeast Pacific provides initial baseline information on ambient noise levels within the region. The time and frequency dependent characteristics of sounds generated by breaking waves in the surf zone, wind induced whitecaps, vessel radiated noise, and marine mammal vocalizations were identified and measured to assess their contributions to ambient noise levels. Over the course of the year, vessel generated noise produced the loudest recorded sound pressure level (152 dB *re* 1 μ Pa) and was a persistent feature often dominating the low frequency acoustic spectrum ($f < 840$ Hz). Surf generated noise has a strong seasonal effect on ambient noise below $f < 100$ Hz, while sound attributed to winds influences ambient levels when speeds reach 10 m/s. Compared with other environmentally energetic sites, the Oregon coast stands out as a high energy end member of surf generated noise in the lower frequencies ($f < 100$ Hz). Additionally, records of vocalizing marine mammals also show time dependent behavior influencing ambient levels in particular frequency bands with the majority of signals occurring in the fall and early winter months (September – December). Finally, selected percentile distributions of spectral levels are used to construct a baseline sound budget for evaluation of noise radiated by future anthropogenic activities on ambient levels.

The results of this dissertation were drawn together by using underwater acoustic techniques and technologies within the spatial framework of the northeast Pacific Ocean to enhance our understanding of [1] seafloor earthquake processes along the boundaries of the intermediate spreading Juan de Fuca plate system, [2] the cycle of increasing seismic energy associated with magma intrusion at Axial Seamount, and [3] provide a quantitative measure of time and source dependent shallow water ambient noise levels.

BIBLIOGRAPHY

- Andrew, R. K., Howe, B. M., Mercer, J. A., and Dzieciuch, M. A., 2002, Ocean ambient sound: comparing the 1960s with the 1990s for a receiver off the California coast: *Acoustics Research Letters Online*, v. 3, no. 2, p. 65-70.
- Au, W. W. L., 1993, *The sonar of dolphins*, (Springer-Verlag, New York Inc.), p. 277.
- Bassett, C., Thomson, J., Polagye, B., and Rhinefrank, K., Underwater noise measurements of a 1/7th scale wave energy converter, In Proceedings of MTS/IEEE OCEANS. Kona, USA. September 2011, p. 1-6.
- Bohnenstiehl, D. R., Dziak, R. P., Tolstoy, M., Fox, C. G., and Fowler, M., 2004a, Temporal and spatial history of the 1999–2000 Endeavour Segment seismic series, Juan de Fuca Ridge: *Geochemistry, Geophysics, Geosystems*, v. 5.
- , 2004b, Temporal and spatial history of the 1999–2000 Endeavour Segment seismic series, Juan de Fuca Ridge: *Geochemistry, Geophysics, Geosystems*, v. 5.
- Bohnenstiehl, D. R., Tolstoy, M., Dziak, R. P., Fox, C. G., and Smith, D. K., 2002, Aftershock sequences in the mid-ocean ridge environment: an analysis using hydroacoustic data: *Tectonophysics*, v. 354, no. 1-2, p. 49-70.
- Braunmiller, J., and Nábělek, J., 2008, Segmentation of the Blanco Transform Fault Zone from earthquake analysis: Complex tectonics of an oceanic transform fault: *Journal of Geophysical Research: Solid Earth (1978–2012)*, v. 113, no. B7.
- Caress, D. W., Clague, D. A., Paduan, J. B., Martin, J. F., Dreyer, B. M., Chadwick Jr, W. W., Denny, A., and Kelley, D. S., 2012, Repeat bathymetric surveys at 1-metre resolution of lava flows erupted at Axial Seamount in April 2011: *Nature Geoscience*, v. 5, no. 7, p. 483-488.
- Chadwick, W. W., Nooner, S. L., Butterfield, D. A., and Lilley, M. D., 2012, Seafloor deformation and forecasts of the April 2011 eruption at Axial Seamount: *Nature Geoscience*, v. 5, no. 7, p. 474-477.
- Chadwick, W. W., Clague, D. A., Embley, R. W., Perfit, M. R., Butterfield, D. A., Caress, D. W., Paduan, J. B., Martin, J. F., Sasnett, P., and Merle, S. G., 2013, The 1998 eruption of Axial Seamount: New insights on submarine lava flow emplacement from high-resolution mapping: *Geochemistry, Geophysics, Geosystems*, in press.
- Chadwick, W. W., Nooner, S. L., Zumberge, M. A., Embley, R. W., and Fox, C. G., 2006, Vertical deformation monitoring at Axial Seamount since its 1998

- eruption using deep-sea pressure sensors: *Journal of Volcanology and Geothermal Research*, v. 150, no. 1-3, p. 313-327.
- Chapman, N. R., and Price, A., 2011, Low frequency deep ocean ambient noise trend in the Northeast Pacific Ocean: *The Journal of the Acoustical Society of America*, v. 129, no. 5, p. EL161-EL165.
- Clark, C. W., Ellison, W. T., Southall, B. L., Hatch, L., Van Parijs, S. M., Frankel, A., and Ponirakis, D., 2009, Acoustic masking in marine ecosystems: intuitions, analysis, and implication: *Marine Ecology Progress Series*, v. 395, p. 201-222.
- Cronin, V. S., and Sverdrup, K. A., 2003, Multiple-event relocation of historic earthquakes along Blanco Transform Fault Zone, NE Pacific: *Geophysical Research Letters*, v. 30, no. 19, p. 2001.
- Cummings, W. C., and Thompson, P. O., 1971, Underwater sounds from the blue whale, *Balaenoptera musculus*: *The Journal of the Acoustical Society of America*, v. 50, p. 1193.
- Davis, E., Becker, K., Dziak, R., Cassidy, J., Wang, K., and Lilley, M., 2004, Hydrological response to a seafloor spreading episode on the Juan de Fuca ridge: *Nature*, v. 430, no. 6997, p. 335-338.
- Deane, G. B., 2000, Long time-base observations of surf noise: *The Journal of the Acoustical Society of America*, v. 107, no. 2, p. 758-770.
- Dziak, R. P., 2001, Empirical relationship of T-wave energy and fault parameters of northeast Pacific Ocean earthquakes: *Geophysical Research Letters*, v. 28, no. 13, p. 2537-2540.
- , 2006, Explorer deformation zone: Evidence of a large shear zone and reorganization of the Pacific–Juan de Fuca–North American triple junction: *Geology*, v. 34, no. 3, p. 213-216.
- Dziak, R. P., Chadwick, W. W., Fox, C. G., and Embley, R. W., 2003, Hydrothermal temperature changes at the southern Juan de Fuca Ridge associated with Mw 6.2 Blanco Transform earthquake: *Geology*, v. 31, no. 2, p. 119-122.
- Dziak, R. P., and Fox, C. G., 1999a, Long-term seismicity and ground deformation at Axial Volcano, Juan de Fuca Ridge: *Geophysical Research Letters*, v. 26, no. 24, p. 3641-3644.
- , 1999b, The January 1998 earthquake swarm at Axial Volcano, Juan de Fuca Ridge: Hydroacoustic evidence of seafloor volcanic activity: *Geophysical Research Letters*, v. 26, no. 23, p. 3429-3432.

- Dziak, R. P., Fox, C. G., and Schreiner, A. E., 1995, The June-July 1993 seismo-acoustic event at CoAxial segment, Juan de Fuca Ridge: Evidence for a lateral dike injection: *Geophysical Research Letters*, v. 22, no. 2, p. 135-138.
- Dziak, R. P., Fox, C. G., and Slack, P. D., 1996, T wave source level and earthquake fault parameters: Empirically derived scaling relationships: *The Journal of the Acoustical Society of America*, v. 100, p. 2639.
- Dziak, R. P., Hammond, S. R., and Fox, C. G., 2011, A 20-year hydroacoustic time series of seismic and volcanic events in the Northeast Pacific Ocean: *Oceanography-Oceanography Society*, v. 24, no. 3, p. 280.
- Dziak, R. P., Haxel, J. H., Bohnenstiehl, D. R., Chadwick, W. W., Nooner, S. L., Fowler, M. J., Matsumoto, H., and Butterfield, D. A., 2012, Seismic precursors and magma ascent before the April 2011 eruption at Axial Seamount: *Nature Geoscience*, v. 5, no. 7, p. 478-482.
- Edds-Walton, P. L., 1997, Acoustic communication signals of mysticete whales: *Bioacoustics*, v. 8, no. 1&2, p. 47-60.
- Einarsson, P., and Brandsdottir, B., 1980, Seismological evidence for lateral magma intrusion during the July 1978 deflation of the Krafla volcano in NE Iceland: *Journal of Geophysics-Zeitschrift Fur Geophysik*, v. 47, no. 1-3, p. 160-165.
- Embley, R. W., Chadwick Jr, W. W., Clague, D., and Stakes, D., 1999, 1998 eruption of axial volcano: Multibeam anomalies and sea-floor observations: *Geophysical Research Letters*, v. 26, no. 23, p. 3425-3428.
- Fox, C. G., Cowen, J. P., Dziak, R. P., Baker, E. T., Embley, R. W., Chadwick, W. W., Lupton, J. E., Resing, J. A., and Hammond, S. R., Detection and response to a seafloor spreading episode on the central Gorda Ridge, April 2001, *in* Proceedings American Geophysical Union 2001 Fall Meeting, San Francisco, CA, 2001a, Volume 1, p. 05.
- Fox, C. G., and Dziak, R. P., 1998, Hydroacoustic detection of volcanic activity on the Gorda Ridge, February–March 1996: *Deep Sea Research Part II: Topical Studies in Oceanography*, v. 45, no. 12, p. 2513-2530.
- , 1999, Internal deformation of the Gorda Plate observed by hydroacoustic monitoring: *Journal of Geophysical Research: Solid Earth (1978–2012)*, v. 104, no. B8, p. 17603-17615.
- Fox, C. G., Matsumoto, H., and Lau, T. K. A., 2001b, Monitoring Pacific Ocean seismicity from an autonomous hydrophone array: *Journal of Geophysical Research*, v. 106, no. B3, p. 4183-4206.

- Fox, C. G., Radford, W. E., Dziak, R. P., Lau, T. K., Matsumoto, H., and Schreiner, A. E., 1995, Acoustic detection of a seafloor spreading episode on the Juan de Fuca Ridge using military hydrophone arrays: *Geophysical Research Letters*, v. 22, no. 2, p. 131-134.
- Frohlich, C., and Davis, S. D., 1990, Single Link Cluster Analysis As A Method to Evaluate Spatial and Temporal Properties of Earthquake Catalogues: *Geophysical Journal International*, v. 100, no. 1, p. 19-32.
- Goltz, C., 2001, Decomposing spatio-temporal seismicity patterns: *Natural Hazards and Earth System Science*, v. 1, no. 1/2, p. 83-92.
- Haxel, J. H., Dziak, R. P., and Matsumoto, H., Obtaining baseline measurements of ocean ambient sound at a mobile test berth site for wave energy conversion off the central Oregon coast, In Proceedings of MTS/IEEE OCEANS. Kona, USA. September 2011, p. 1-5.
- Herzing, D. L., and Mate, B. R., 1984, Gray whale (*Eschrichtius robustus*) migrations along the Oregon coast, In *The Gray Whale, Eschrichtius Robustus*, edited by J. S. L. M.L. Jones, and S.L. Swartz (Academic Press Inc., New York), pp. 289-307.
- Hildebrand, J. A., 2009, Anthropogenic and natural sources of ambient noise in the ocean: *Marine Ecology-Progress Series*, v. 395, p. 5-20.
- Holliday, J. R., Chen, C.-c., Tiampo, K. F., Rundle, J. B., Turcotte, D. L., and Donnellan, A., 2007, A RELM earthquake forecast based on pattern informatics: *Seismological Research Letters*, v. 78, no. 1, p. 87-93.
- Kasumyan, A. O., 2008, Sounds and sound production in fishes: *Journal of Ichthyology*, v. 48, no. 11, p. 981-1030.
- Knudsen, V. O., Alford, R., and Emling, J., 1948, Underwater ambient noise: *Journal of Marine Research*, v. 7, no. 3, p. 410-429.
- McDonald, M. A., Hildebrand, J. A., and Wiggins, S. M., 2006, Increases in deep ocean ambient noise in the northeast Pacific west of San Nicolas Island, California: *The Journal of the Acoustical Society of America*, v. 120, no. 2, p. 711-718.
- McDonald, M. A., Hildebrand, J. A., Wiggins, S. M., and Ross, D., 2008, A 50 year comparison of ambient ocean noise near San Clemente Island: A bathymetrically complex coastal region off Southern California: *The Journal of the Acoustical Society of America*, v. 124, p. 1985.

- Medwin, H., and Beaky, M. M., 1989, Bubble sources of the Knudsen sea noise spectra: *The Journal of the Acoustical Society of America*, v. 86, p. 1124.
- Mellinger, D. K., 2001, Ishmael 1.0 user's guide: NOAA Technical Memorandum OAR PMEL, v. 120, no. 26, p. 98115-96349.
- NRC (National Research Council), 2005, *Marine Mammal Populations and Ocean Noise: Determining When Noise Causes Biologically Significant Effects*. (National Academy Press), p. 126.
- Nooner, S. L., and Chadwick, W. W., 2009, Volcanic inflation measured in the caldera of Axial Seamount: Implications for magma supply and future eruptions: *Geochemistry Geophysics Geosystems*, v. 10.
- Nystuen, J. A., 1986, Rainfall measurements using underwater ambient noise: *The Journal of the Acoustical Society of America*, v. 79, p. 972.
- Pedersen, R., Sigmundsson, F., and Einarsson, P., 2007, Controlling factors on earthquake swarms associated with magmatic intrusions; Constraints from Iceland: *Journal of Volcanology and Geothermal Research*, v. 162, no. 1-2, p. 73-80.
- Picciulin, M., Sebastianutto, L., Codarin, A., Farina, A., and Ferrero, E. A., 2010, In situ behavioural responses to boat noise exposure of *Gobius cruentatus* and *Chromis chromis* living in a Marine Protected Area: *Journal of Experimental Marine Biology and Ecology*, v. 386, no. 1, p. 125-132.
- Piggott, C., 1964, Ambient sea noise at low frequencies in shallow water of the Scotian Shelf: *The Journal of the Acoustical Society of America*, v. 36, no. 11, p. 2152-2163.
- Preisendorfer, R. W., and Mobley, C. D., 1988, Principal component analysis in meteorology and oceanography, 425 pp, Elsevier Sci., New York.
- Prosperetti, A., and Oguz, H. N., 1993, The impact of drops on liquid surfaces and the underwater noise of rain: *Annual review of fluid mechanics*, v. 25, no. 1, p. 577-602.
- Rivers, J. A., 1997, Blue whale, *Balaenoptera musculus*, vocalizations from the waters off central California: *Marine Mammal Science*, v. 13, no. 2, p. 186-195.
- Ross, D., 1976, Mechanics of underwater sound, *Mechanics of Underwater Noise* (Pergamon Press, New York), p. 375.

- Rundle, J. B., Klein, W., Tiampo, K., and Gross, S., 2000, Linear pattern dynamics in nonlinear threshold systems: *Physical Review E*, v. 61, no. 3, p. 2418.
- Saenger, R. A., 1961, An estimate of the offshore ambient noise spectrum produced by pounding surf: *The Journal of the Acoustical Society of America*, v. 33, p. 1674.
- Simpson, S. D., Meekan, M., Montgomery, J., McCauley, R., and Jeffs, A., 2005, Homeward sound: *Science*, v. 308, no. 5719, p. 221-221.
- Sohn, R. A., Barclay, A. H., and Webb, S. C., 2004, Microearthquake patterns following the 1998 eruption of Axial Volcano, Juan de Fuca Ridge: Mechanical relaxation and thermal strain: *Journal of Geophysical Research-Solid Earth*, v. 109, no. B1, p. 14.
- Sohn, R. A., Crawford, W. C., and Webb, S. C., 1999, Local seismicity following the 1998 eruption of Axial Volcano: *Geophysical Research Letters*, v. 26, no. 23, p. 3433-3436.
- Southall, B., Bowles, A., Ellison, W., Finneran, J., Gentry, R., Greene, C., Kastak, D., Ketten, D., Miller, J., and Nachtigall, P., 2007, Marine mammal noise exposure criteria: Initial scientific recommendations," *Aquatic Mammals*, 33, 411-521.
- Strasberg, M., 1979, Nonacoustic noise interference in measurements of infrasonic ambient noise: *The Journal of the Acoustical Society of America*, v. 66, p. 1487.
- Sturkell, E., Sigmundsson, F., and Einarsson, P., 2003, Recent unrest and magma movements at Eyjafjallajökull and Katla volcanoes, Iceland: *Journal of Geophysical Research*, v. 108, no. B8, p. 2369.
- Teague, W. J., Carron, M. J., and Hogan, P. J., 1990, A comparison between the Generalized Digital Environmental Model and Levitus climatologies: *Journal of Geophysical Research: Oceans* (1978–2012), v. 95, no. C5, p. 7167-7183.
- Tiampo, K. F., Rundle, J. B., McGinnis, S. A., and Klein, W., 2002, Pattern dynamics and forecast methods in seismically active regions: *Pure and Applied Geophysics*, v. 159, p. 2429-2467.
- Tolstoy, I., and Ewing, M., 1950, The T phase of shallow-focus earthquakes: *Bulletin of the Seismological Society of America*, v. 40, no. 1, p. 25.
- Tolstoy, M., Vernon, F. L., Orcutt, J. A., and Wyatt, F. K., 2002, Breathing of the seafloor: Tidal correlations of seismicity at Axial volcano: *Geology*, v. 30, no. 6, p. 503-506.

- Tryggvason, E., 1994, Surface deformation at the Krafla volcano, North Iceland, 1982-1992: *Bulletin of Volcanology*, v. 56, no. 2, p. 98-107.
- Tyack, P., 1981, Interactions between singing Hawaiian humpback whales and conspecifics nearby: *Behavioral Ecology and Sociobiology*, v. 8, no. 2, p. 105-116.
- Tyack, P. L., and Clark, C. W., 2000, Communication and acoustic behavior of dolphins and whales: In *Hearing by Whales and Dolphins*, edited by Au, W.L., Popper, A.N., and Fay, R.R., Springer Handbook of Auditory Research Series 12, p. 156-224.
- Vagle, S., Large, W. G., and Farmer, D. M., 1990, An evaluation of the WOTAN technique of inferring oceanic winds from underwater ambient sound: *Journal of Atmospheric and Oceanic Technology*, v. 7, p. 576-595.
- Watkins, W. A., Tyack, P., Moore, K. E., and Bird, J. E., 1987, The 20-Hz signals of finback whales (*Balaenoptera physalus*): *The Journal of the Acoustical Society of America*, v. 82, no. 6, p. 1901-1912.
- Wenz, G. M., 1962, Acoustic ambient noise in the ocean: spectra and sources: *The Journal of the Acoustical Society of America*, v. 34, p. 1936.
- , 1964, Ambient noise measurements west of San Clemente Island, U.S. Navy Electronics Laboratory Report 1235, p. 46.
- West, M., Menke, W., Tolstoy, M., Webb, S., and Sohn, R., 2001, Magma storage beneath Axial volcano on the Juan de Fuca mid-ocean ridge: *Nature*, v. 413, no. 6858, p. 833-836.
- Wilson Jr, O., Wolf, S. N., and Ingenito, F., 1985, Measurements of acoustic ambient noise in shallow water due to breaking surf: *The Journal of the Acoustical Society of America*, v. 78, p. 190.
- Wilson, O. B., Stewart, M. S., Wilson, J. H., and Bourke, R. H., 1997, Noise source level density due to surf. I. Monterey Bay, CA: *IEEE Journal of Oceanic Engineering*, v. 22, no. 3, p. 425-433.
- Wladichuk, J. L., Megill, W. M., and Blondel, P., 2008, Passive acoustic localization techniques of Eastern Pacific grey whales: *The Journal of the Acoustical Society of America*, v. 123, no. 5, p. 3207.
- Wright, A. J., Soto, N. A., Baldwin, A. L., Bateson, M., Beale, C. M., Clark, C., Deak, T., Edwards, E. F., Fernández, A., and Godinho, A., 2007, Do Marine

Mammals Experience Stress Related to Anthropogenic Noise?: *International Journal of Comparative Psychology*, v. 20, no. 2.

Wright, T. J., Sigmundsson, F., Pagli, C., Belachew, M., Hamling, I. J., Brandsdóttir, B., Keir, D., Pedersen, R., Ayele, A., and Ebinger, C., 2012, Geophysical constraints on the dynamics of spreading centres from rifting episodes on land: *Nature Geoscience*, v. 5, no. 4, p. 242-250.